Research Article

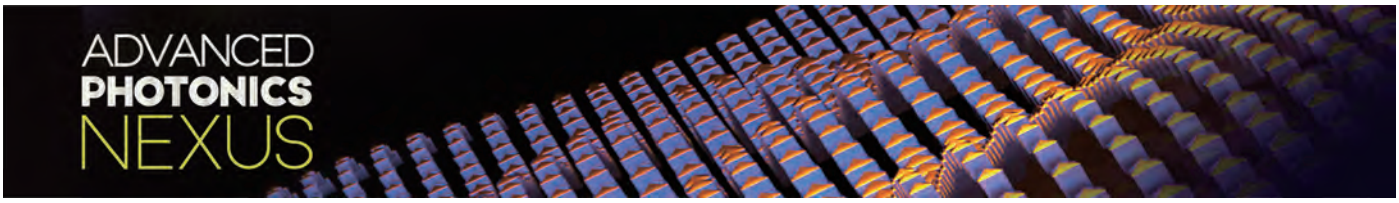

Achieving higher photoabsorption than group III-V semiconductors in ultrafast thin silicon photodetectors with integrated photon-trapping surface structures

Wayesh Qarony,[a,†] Ahmed S. Mayet,[a,†] Ekaterina Ponizovskaya Devine,[b] Soroush Ghandiparsi,[a] Cesar Bartolo-Perez,[a] Ahasan Ahamed,[a] Amita Rawat,[a] Hasina H. Mamtaz,[a] Toshishige Yamada,[b,c] Shih-Yuan Wang,[b] and M. Saif Islam[a,*]

[a]University of California, Davis, Department of Electrical and Computer Engineering, Davis, California, United States
[b]W&WSens Devices, Inc., Los Altos, California, United States
[c]University of California, Baskin School of Engineering, Department of Electrical and Computer Engineering, Santa Cruz, California, United States

Abstract. The photosensitivity of silicon is inherently very low in the visible electromagnetic spectrum, and it drops rapidly beyond 800 nm in near-infrared wavelengths. We have experimentally demonstrated a technique utilizing photon-trapping surface structures to show a prodigious improvement of photoabsorption in 1-μm-thin silicon, surpassing the inherent absorption efficiency of gallium arsenide for a broad spectrum. The photon-trapping structures allow the bending of normally incident light by almost 90 deg to transform into laterally propagating modes along the silicon plane. Consequently, the propagation length of light increases, contributing to more than one order of magnitude improvement in absorption efficiency in photodetectors. This high-absorption phenomenon is explained by finite-difference time-domain analysis, where we show an enhanced photon density of states while substantially reducing the optical group velocity of light compared to silicon without photon-trapping structures, leading to significantly enhanced light–matter interactions. Our simulations also predict an enhanced absorption efficiency of photodetectors designed using 30- and 100-nm silicon thin films that are compatible with CMOS electronics. Despite a very thin absorption layer, such photon-trapping structures can enable high-efficiency and high-speed photodetectors needed in ultrafast computer networks, data communication, and imaging systems, with the potential to revolutionize on-chip logic and optoelectronic integration.

Keywords: photoabsorption; photon trapping; group-velocity reduction; photodetectors; silicon photonics.

Received May 19, 2023; revised manuscript received Jun. 22, 2023; accepted for publication Jul. 3, 2023; published online Jul. 24, 2023.

[DOI: 10.1117/1.APN.2.5.056001]

1 Introduction

Emerging applications in cloud computing, optical communication and interconnects,[1–4] internet of things (IoT) integrated communication networks,[5,6] lidar-assisted applications, such as autonomous vehicles,[7] security, surveillance, artificial intelligence,[8,9] and low-light-enabled imaging applications in life sciences[10–12] can be made economical and versatile by designing complementary metal-oxide-semiconductor (CMOS)-compatible or silicon (Si)-compatible photonic systems. However, as an indirect bandgap material, Si inherently exhibits a weaker absorption coefficient in comparison to group III-V compound semiconductors.[13,14] The absorption in Si shows a dramatic

*Address all correspondence to M. Saif Islam, sislam@ucdavis.edu
†These authors contributed equally to this work.

reduction in the near-infrared (NIR) wavelength spectrum—a wavelength spectrum range essential to plenty of the aforementioned optoelectronic applications. Owing to its weak absorption, Si-based photonic devices demand a thick substrate layer to fully utilize the illuminated optical stimuli, e.g., for 95% photon absorption of 850 nm wavelength, a ∼50 μm thick Si layer is required.[15] Despite an enhanced absorption in such a thick Si absorption layer, a long transit time of the generated electron–hole pair and its inherent low carrier mobilities result in only sub-par photodetectors that do not comply with the performance requirements of emerging photonic systems. In contrast with Si, the most commonly used III-V compounds, such as GaAs and InP, exhibit 15× and 40× higher absorption, respectively, at a wavelength of 850 nm.[13] GaAs shows ∼90% absorption of 850 nm incident wavelength in merely a 2.5 μm thick layer. Attributing to its higher absorption coefficient and exceptionally high carrier mobilities,[16] GaAs-based photodetectors exceed the performance expectations for the current and emerging optoelectronic systems. Such exceptional performance helps the GaAs, and their alloys thrive as the mainstream materials for numerous emerging photonic applications. However, a CMOS incompatibility in the fabrication process of such devices calls for a tedious and costly hybrid integration with CMOS electronics. Recently, despite its sub-par performance, foundries have introduced Si-based optoelectronic integrated circuits in the CMOS infrastructure[17,18] as a trade-off between performance and the manufacturing/integration cost. Therefore, innovative techniques to enhance light–matter interaction are crucial to designing photodetectors with diminishingly thin Si films used in modern CMOS processes.

Researchers are actively working on engineering photon-trapping solar cells and light-emitting diodes with diffusive surface textures to enable randomized light scattering and have demonstrated considerable enhancement in efficiency.[15,19–23] The most recent studies focus on theoretical simulations of the integrated photon-trapping structures in solar cells, offering distinctly high-absorption efficiency by generating enhanced photonic density of states (DOS) and guided optical modes.[24–30] These simulations utilize the wave optics approach, which applies realistic Maxwell's physics as opposed to the geometric optics to simulate a thin-film solar cell and show an enhancement in the effective optical path length that absorbs close to or beyond the geometrical limit. Different wave optics photon-trapping schemes, such as photonic crystal structures,[31,32] metallic nanoparticles,[33] plasmonic surfaces,[34,35] and grating,[36] have been extensively investigated. Many of these theoretical investigations have revealed a very high optical absorption enhancement enabled by the photonic light-trapping structures in Si solar cells at longer illumination wavelengths.[26,37,38] With the emergence of advanced optical device design and fabrication techniques, several experimental demonstrations of high optical absorption efficiency in solar cells and photodiodes have been conducted.[39–44] However, we were the first to experimentally demonstrate high-efficiency and ultrafast Si photodetectors operating in the NIR regime by integrating photon-trapping microhole structures.[45] Later, several similar techniques with such microhole structures were utilized in realizing efficient and ultrafast photodetectors, avalanche photodetectors, and high-performance single-photon avalanche photodetectors.[46–49] It should be noted that photodetectors usually operate under reverse bias conditions, while solar cells are designed to operate at maximum power points and are used under zero bias. To circumvent the arduous device fabrication processes, researchers measured the quantum efficiencies using $1-T-R$, where T and R are transmission and reflection of the illuminated light.[20,21,24] In contrast, the quantum efficiencies of photodetectors were directly calculated from the measured $I-V$ characteristics. Despite tremendous development in the fabrication facilities, such prodigious absorption enhancement in Si is only theoretically demonstrated and yet to be experimentally realized.[21,50]

In this work, we report an experimental demonstration of the performance enhancement of an Si photodetector by incorporating photon-trapping micro- and nanosurface structures. We have fabricated metal–semiconductor–metal (MSM) photodetector on a 1 μm thin Si layer and integrated periodic photon-trapping hole arrays. We have utilized CMOS-compatible processes to fabricate the photodetectors. To present a fair comparison, we have fabricated two sets of devices with and without a photon-trapping hole array. These hole arrays assist in diverting normally incident beams of light almost orthogonally and facilitate a lateral propagation of light. Such engineered surface profiling efficiently guides and effectively slows down the propagating light beam and results in a dramatic improvement in absorption efficiency. We demonstrate remarkable enhancement of 80%, 85%, and 65% in the absorption efficiency in the photon-trapping-equipped photodetectors for the NIR wavelength spectrum at 800, 850, and 905 nm, respectively. Further, we show a ∼20% reduction in the device capacitance due to a reduced effective device volume of photon-trapping-equipped Si photodetectors that can further result in ultrafast performance due to the reduction in the resistance and capacitance (RC) time constant.[51]

Furthermore, with the help of finite-difference time-domain (FDTD) simulations, we have shown that most of the propagating modes in Si with photon-trapping structures exhibit lower optical group velocity compared to that of the conventional Si layer without photon-trapping structures. This contributes to enhanced light–matter interaction, ensuring a higher absorption. This enhancement in the absorption is shown to be comparable to that of GaAs absorption. We have also shown that an equivalent performance enhancement can be achieved with 30 and 100 nm thin Si layers. The performance of such ultrathin Si-based photo-trapping-equipped photodetectors are intriguingly encouraging for fabricating ultrafast photodetectors in the existing CMOS foundry framework.[52,53]

2 Fabrication of the Photodetectors on a 1 μm Thin Si Layer

A thin Si slab with a thickness of 1 μm integrated with a photon-trapping structure of cylindrical shape is designed to maximize light absorption. In this effort, the geometry is optimized for the lattice structure, diameter, period, and depth of the photon-trapping holes that are filled with air. The cross-sectional structure is schematically shown in Fig. 1(a) and Figs. S2 and S7 in the Supplementary Material. To fabricate the photodetectors, we have exploited the standard CMOS-compatible infrastructure. We have opted for a mesa-based photodetector geometry where the photon trapping holes are patterned on the top mesa. The devices are fabricated on a silicon-on-insulator (SOI) substrate with a 1 μm thick active Si layer (the absorber layer). Figure 1(b) showcases the optical micrographs of the fabricated photodetectors for a range of hole diameter (d) and periodicity (p). Detailed microscopic images of the fabricated device are shown in Fig. S3 in the Supplementary Material. A firsthand

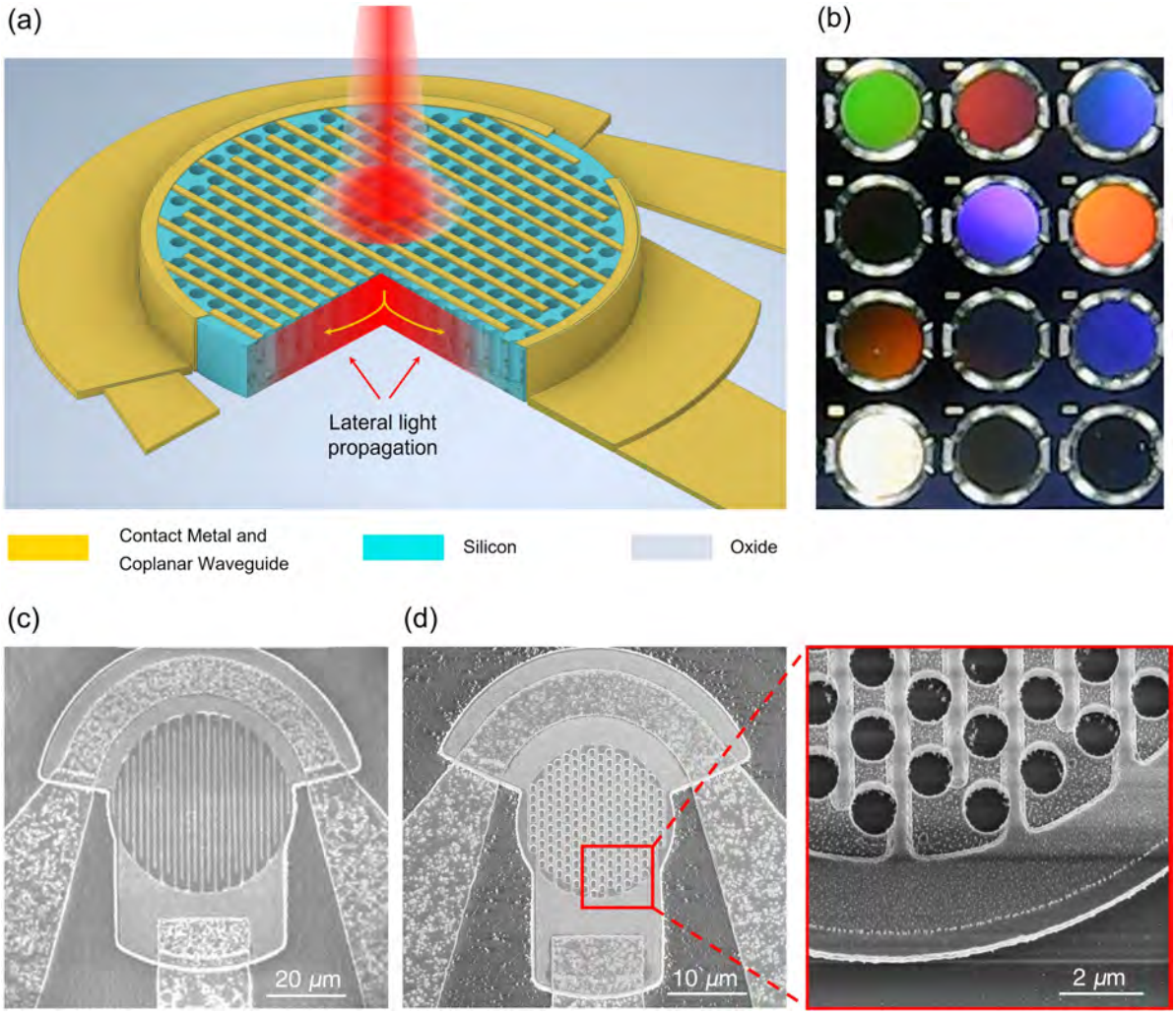

Fig. 1 Design and fabrication of highly absorbing thin-film Si photon-trapping photodetector. (a) Schematic of the photon-trapping silicon MSM photodetector. The photon-trapping cylindrical hole arrays allow lateral propagation by bending the incident light, resulting in an enhanced photon absorption in Si. (b) Optical microscopy images of the photon-trapping photodetectors fabricated on a 1 μm thin Si layer of the SOI substrate for a range of hole diameters, d, and period, p of the holes. Under white light illuminations, the flat devices look white (bottom left) because of surface reflection. The most effective photon-trapping device looks black (bottom right). Less effective photon-trapping devices show different colors reflected from the surface of the devices. SEM images of fabricated (c) planar and (d) photon-trapping MSM photodetectors. The inset indicates circular-shaped holes in a hexagonal lattice formation (Video 1, mp4, 5.27 MB [URL: https://doi.org/10.1117/1.APN.2.5.056001.s1]).

confirmation of the wavelength selectivity of these photon-trapping holes is evident from the different color spectra revealed during microscopic imaging for different devices with different d and p [Fig. 1(b)]. The scanning electron microscopy (SEM) images of the planar and photon-trapping photodetectors are shown in Figs. 1(c) and 1(d), respectively. The planar (without holes) photodetectors are used as a control device to benchmark the performance enhancement resulting from the hole-array introduction. The inset of Fig. 1(d) indicates that the patterned holes are circular. Interdigitated aluminum fingers with a thickness of 100 nm and width of 300 nm are sputtered on Si. Cylindrical photon-trapping holes with a p, d, and hole depth of 1300, 1000, and 600 nm, respectively, are etched in the Si active layer. Fabricated photodetectors are isolated from each other, and coplanar waveguides (CPWs) were delineated for high-speed operation. The roughness observed on the CPW pads and the presence of residual dielectric particles on the Si surface were a result of the hydrofluoric acid (HF) passivation process during fabrication. Despite these effects, the optical measurement remained unaffected. The details of the fabrication method are discussed in Fig. S1 in the Supplementary Material.[47]

3 Leapfrogging the Absorption Coefficient of Thin Si beyond That of Intrinsic GaAs

Using the Bouguer–Beer–Lambert law and considering surface reflection losses,[54,55] an effective absorption coefficient (α_{eff}),

defined in Eq. (1), is estimated to quantify the enhancement in photon absorption of the fabricated devices with photon-trapping structures,

$$\alpha_{\text{eff}}(\lambda) = -\frac{1}{t_{\text{Si}}}\left\{\ln\left[\frac{1-\text{QE}_{\text{meas}}(\lambda)}{1-R_{\text{meas}}(\lambda)}\right]\right\}, \quad (1)$$

where t_{Si} is the thickness of the Si active layer of the photodetector, and QE_{meas} and R_{meas} are the experimentally measured quantum efficiency (QE) and surface reflection of the devices, respectively. If a perfect photon absorption is assumed with a QE close to unity or 100% in a thin semiconductor film, the enhanced absorption efficiency (α_{eff}) approaches an exceptionally high value. The measured surface reflections for the planar devices without antireflection coating range from 15% to 25%, whereas the surface reflections in the case of photon-trapping photodetectors show a notable reduction and are measured to be from 10% to 12% for illumination wavelengths ranging from 800 to 905 nm. Using the experimental results and Eq. (1), the α_{eff} of the Si photon-trapping photodetectors is estimated as a function of incident wavelengths. The estimated α_{eff} of the photon-trapping thin Si photodetectors is compared against the absorption coefficient of the bulk Si and other potential photosensitive semiconductors, such as Ge,[56] InGaAs,[56] and GaAs,[57] as shown in Fig. 2(a). The enhancement factor of the 1 μm thin photon-trapping Si photodetectors is not only higher than that of the bulk Si but also exceeds the absorption coefficient of GaAs over a broad NIR wavelength spectrum and becomes comparable to the absorption coefficients of Ge and InGaAs. Quantitatively, in the photon-trapping hole-array-equipped

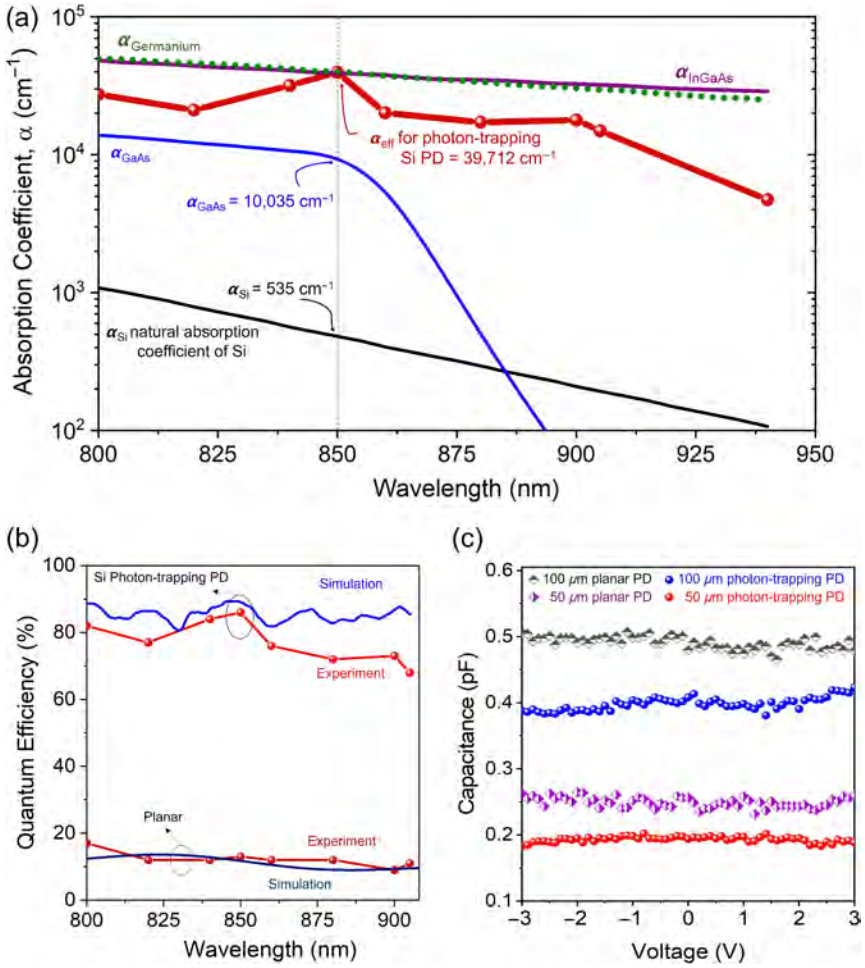

Fig. 2 Experimental demonstration of absorption enhancement in Si that exceeds the intrinsic absorption limit of GaAs. (a) Comparison of the enhanced absorption coefficients (α_{eff}) of the Si photon-trapping photodetectors and the intrinsic absorption coefficients of Si (bulk),[57] GaAs,[57] Ge,[56] and $In_{0.52}Ga_{0.48}As$.[56] The absorption coefficient of engineered photodetectors (PD) shows an increase of 20× at 850 nm wavelength compared to bulk Si, exceeds the intrinsic absorption coefficient of GaAs, and approaches the values of the intrinsic absorption coefficients of Ge and InGaAs. (b) The measured quantum efficiencies of the Si devices have an excellent agreement with FDTD simulation in both planar and photon-trapping devices. (c) Photon-trapping photodetectors exhibit reduced capacitance compared to their planar counterpart, enhancing the ultrafast photoresponse capability of the device (Video 2, mp4, 9.68 MB [URL: https://doi.org/10.1117/1.APN.2.5.056001.s2]).

photodetectors with the measured quantum efficiencies of 80%, 84%, 86%, and 68% at 800, 840, 850, and 905 nm, respectively, α_{eff} is determined to be ~27,467, 31,797, 39,713, and 14,938 cm^{-1}. The α_{eff} determined at 850 nm is more than 70× and about 4× higher than the intrinsic absorption coefficient of Si (535 cm^{-1}) and GaAs (10,035 cm^{-1}),[57] respectively. Hence, the effective absorption coefficient of the fabricated photon-trapping photodetectors exceeded the intrinsic absorption coefficient of GaAs in the NIR wavelength region.

Next, we study QE, an essential performance metric to quantify the optical sensitivity of the fabricated photodetectors. The measured QE of photon-trapping photodetectors for incident wavelengths ranging from 800 to 905 nm is shown in Fig. 2(b). We have shown a comparison of QEs of planar and photon-trapping photodetectors. External quantum efficiencies over 80% are observed experimentally in the photon-trapping photodetectors for incident wavelengths below 860 nm. Owing to Si's inherent optical material properties, the absorption decreases sharply above 860 nm wavelength, with a minimum value as low as 68% at 905 nm. However, compared to the photodetectors with a planar surface, the absorption efficiency is increased by >550% in photon-trapping photodetectors at 850 nm wavelength. The corresponding responsivities of the photon-trapping devices exhibit more than 500 mA/W, as shown in Fig. S11 in the Supplementary Material. In addition, the minimum enhancement of QE in all the fabricated photon-trapping photodetectors compared to the planar devices is at least more than 280% for the wavelength spectrum between 800 and 905 nm. The measured QEs also exhibit an excellent agreement with simulated QEs in both planar and photon-trapping devices, as depicted in Fig. 2(b). The detailed simulation study is discussed in the following section and in the Supplementary Material. Such a high-absorption enhancement directly results from the generation of optical modes propagating laterally due to the integrated photon-trapping surface structures (Video 2). Notably, such photon-trapping photodetectors exhibit reduced capacitance compared to their planar counterpart due to reduced surface areas caused by the photon-trapping structures, as experimentally characterized and depicted in Fig. 2(c), leading to enhance bandwidth in the device. Such reduction in capacitance can further strengthen the ultrafast response of the devices caused by the thin absorption layer. The corresponding dark current of the planar and the photon-trapping devices are also provided in Fig. S10 in the Supplementary Material. So far, to the best of our knowledge, such a high-photoabsorption enhancement in the Si photodetector is the first experimental demonstration.

4 Performance Prediction for Ultrathin Photon-Trapping Si Photodetectors

Leaping on the experimental demonstration of extraordinary enhancement in the performance of photon-trapping photodetectors fabricated on 1 μm thin Si, optical simulations are performed by an FDTD method for the most optimized photon-trapping structure with a p, d, and depth of 1000, 700, and 600 nm, respectively. Again, it should be mentioned here that the best dimension for the fabricated devices was $p = 1300$ nm, $d = 1000$ nm, and depth $= 600$ nm. The discrepancy could occur due to the limitations of the fabrication technologies.[51] The detail of the optical simulation method is provided in the Supplementary Material. Such a photon-trapping structure is simulated for absorption in the wavelengths ranging from 800 to 1100 nm, as presented in Fig. 3(a). Photon-trapping structures with different lattice patterns and microhole shapes/channels also demonstrate a high-absorbing phenomenon, as provided in Figs. S8 and S9 in the Supplementary Material. Figure S9 in the Supplementary Material further demonstrates that different photon-trapping holes with different shapes would impact light–matter interactions in photodetectors differently. Additionally, a Si slab with a 1 μm thickness and a planar surface is also simulated as a reference. The red curve represents simulated absorption spectra of the photon-trapping structure for normally incident light. The photon-trapping structure exhibits distinctly higher absorption in comparison with the planar structure. For Si structure with photon-trapping holes and the normally incident light illumination, a maximum photon absorption exceeding 85% is achieved around the 850 nm wavelength. The photon-trapping structures facilitate absorption enhancement through guided lateral modes for a broad range of NIR wavelengths. Figures 3(b) and 3(c) represent the calculated Poynting vector in the photon-trapping Si slab with 1 μm thickness on the $x - y$ and $x - z$ planes. These figures demonstrate how an ensemble of integrated holes induces a change in the direction of the propagating photons from vertical to lateral orientation in Si films. Laterally oriented Poynting vectors form vortex-like circulation patterns around the sidewalls of the cylindrical holes, resulting in guided light propagation parallel to the photodetector surface for a prolonged time and enabling absorption in Si with high efficiency. Notably, the guided lateral modes in the Si active layer are also facilitated by the front and the back air/Si and Si/oxide layer interfaces, where the oxide layer of the SOI acts as a back reflector. It should be explicitly mentioned here that the oxide layer significantly facilitates the high absorption of photons in the active layer.[51] A movie demonstrating the side view of energy density distribution mapping of a normally incident light beam that bends almost at a right angle into laterally propagating modes of light along the plane of the Si absorber layer with photon-trapping holes is provided in Video 2. To summarize, the photon-trapping surface structures increase the optical path length, which improves the absorption efficiency within the structure with the aid of enhanced light–matter interactions.

To study and analyze the photon absorption limits of ultrathin Si films used in modern CMOS processes, we further explored the absorption efficiency of 30 and 100 nm ultrathin Si films integrated with and without photon-trapping structures, as depicted in Fig. 3(d). Similar to the Si film with 1000 nm thickness, photon-trapping ultrathin Si film exhibits dramatically higher absorption efficiency than the planar Si film. This also proves that such enhancement in absorption is a direct consequence of enhanced light–matter interaction, irrespective of the film thickness, as visualized by Video 3. More than 21% and 8% absorption efficiencies are observed at 850 nm illumination wavelength in Si with 100 and 30 nm absorption thickness, respectively. In contrast, the absorption efficiency is <1% for such ultrathin planar Si, as depicted in Fig. 3(d). The estimated α_{eff} for 100 and 30 nm Si layers are 23,572 and 27,794 cm^{-1}, respectively, which are significantly higher than the intrinsic absorption limit of GaAs at 850 nm wavelength.

Intriguingly, we also observed that the enhanced absorption coefficient of our fabricated devices effectively exceeds the $4n^2$ limit, as provided in Fig. S12 in the Supplementary Material, where n is the refractive index of Si at the corresponding wavelengths. Nevertheless, we cannot claim that it exceeds the

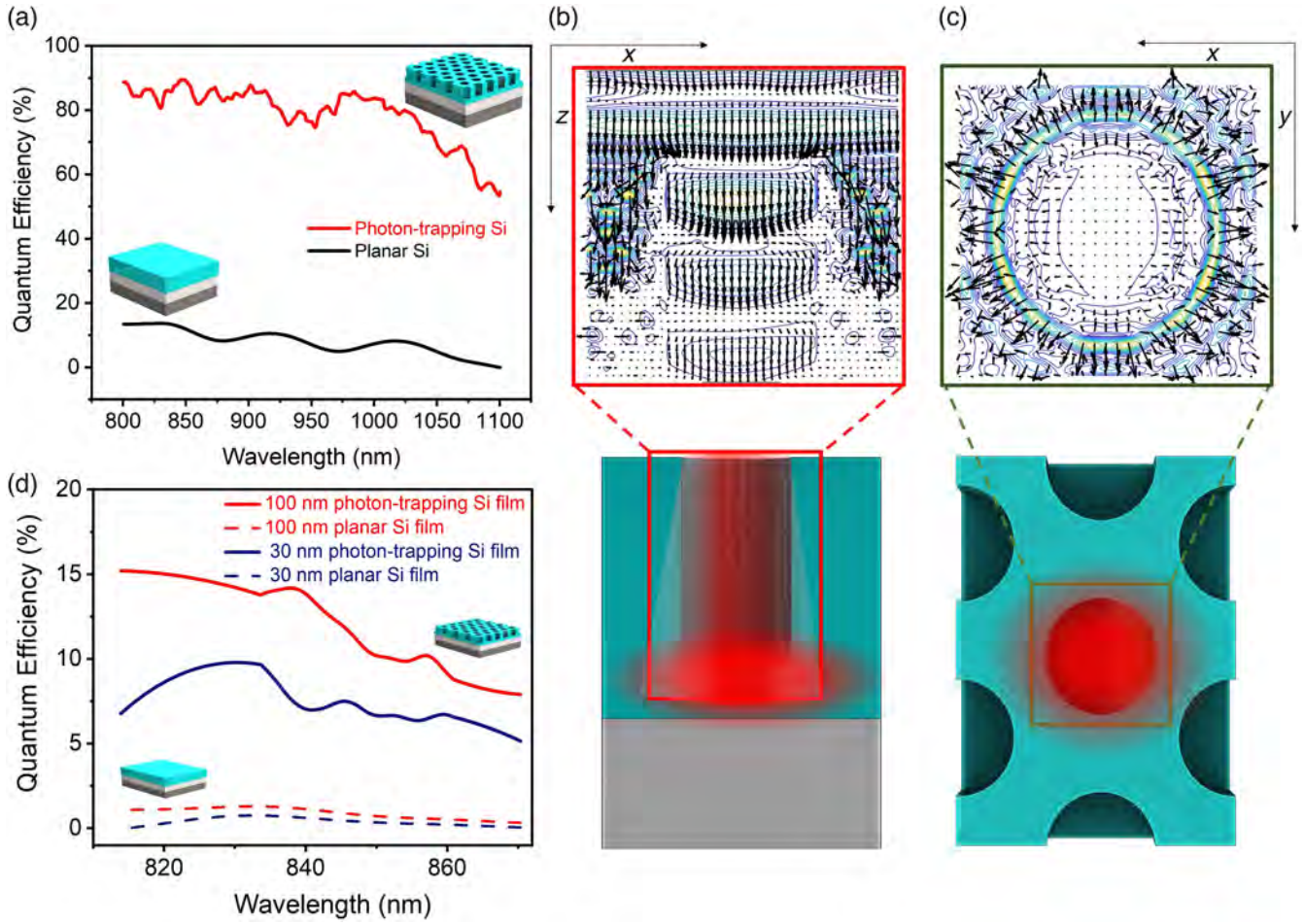

Fig. 3 Theoretical demonstration of enhanced absorption characteristics in ultrathin Si film integrated with photon-trapping structures. (a) Comparison of simulated absorption of photon-trapping [Fig. 1(a) and Fig. S7 in the Supplementary Material] and planar structures demonstrates absorption efficiency in photon-trapping Si around 90% in 1 μm thickness. In contrast, the black curve shows extremely low-absorption efficiency in planar Si without such surface structures. Calculated Poynting vectors in holey 1 μm thin Si on (b) $x-z$ (cross section) and (c) $x-y$ (top view) planes showing that the vectors originated from the hole and moved laterally to the Si sidewalls, where the photons are absorbed. (d) Simulated enhanced optical absorption in ultrathin Si of 30 and 100 nm thicknesses with and without photon-trapping structures.

light-trapping geometrical limit of $4n^2$,[15,19] since a collimated laser beam was used for device illumination. In contrast, an isotropic and incoherent light source is commonly used in solar cell characterization. For the case of a collimated beam, the geometrical limit is adjusted by $4n^2/(\sin\theta)^2$, where θ is the angle between the light source and a plane perpendicular to the surface.[27] We further noticed that the absorption enhancement of our devices could reach a maximum up to $70n^2$ limit at 850 nm of incident wavelength (Fig. S12 in the Supplementary Material). Further investigation correlating the illumination angle of the collimated beams and absorption enhancement will help us understand whether the light-trapping geometrical limit can be overcome.

5 Physics-Based Explanation for the Performance Enhancement

Based on the above observations, photon-trapping structures effectively supporting lateral modes and efficient coupling of light are essential for the optimum enhancement of absorption efficiency. The eigenmodes of the microhole array determine the propagation of photons in the lateral direction. The calculated band structures and allowable available eigenmodes with small holes ($d = 100$ nm, $p = 1000$ nm, and thickness, $t_{Si} = 1000$ nm) and large holes ($d = 700$ nm, $p = 1000$ nm, and thickness, $t_{Si} = 1000$ nm) are shown in Figs. 4(a) and 4(b) and Fig. S14 in the Supplementary Material for the lateral light propagation in a thin film with an array of holes with the period p and hole size d. The band structure is calculated using the standard technique that converts Maxwell's equations from (r, t) space into (k, ω) space by solving the number of wave vectors $k = mp$, where m is an integer number. The eigenmodes in the array were calculated at wavelengths near 850 nm, whereas the ratio of hole diameter to period of the photon-trapping photodetectors is assumed to be $d/p \approx 0.7$ to make it consistent with the fabricated devices. The number of eigenmodes for the hole-array structures increases with an increasing value

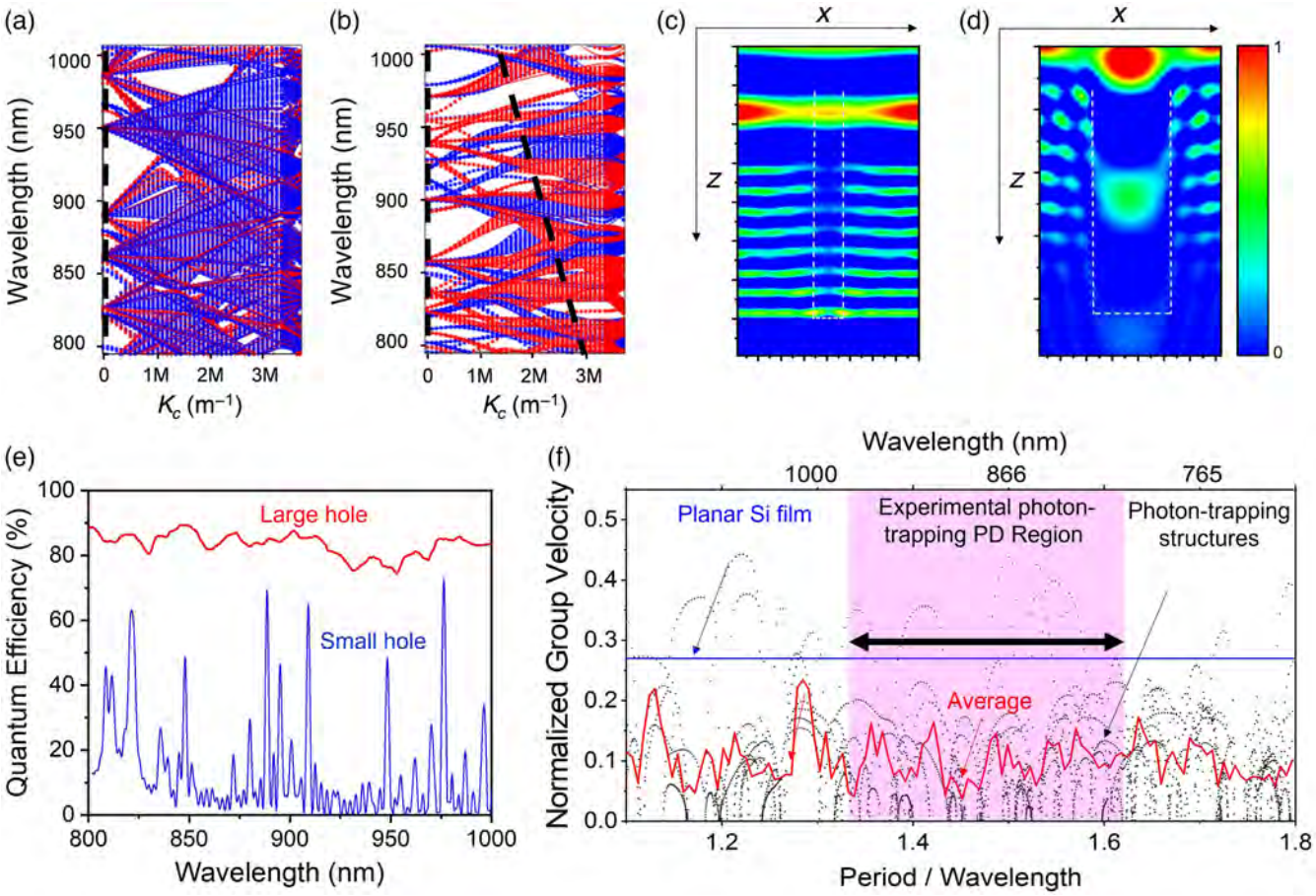

Fig. 4 Reduced group velocity in photon-trapping Si (slow light) and enhanced optical coupling to lateral modes contribute to enhanced photon absorption. Calculated band structure of Si film with (a) small holes ($d = 100$ nm, $p = 1000$ nm, and thickness, $t_{Si} = 1000$ nm) and (b) large holes ($d = 700$ nm, $p = 1000$ nm, and thickness, $t_{Si} = 1000$ nm). Red curves represent TE modes and blue curves represent TM modes. Slanted dashed lines are solutions for k_c that couple into the lateral propagation for a vertically illuminating light source. Small hole structures exhibit solutions only for the finite number of the eigenmodes with $k = 0$ (vertical dashed line), whereas large hole structures essentially have both solutions $k = k_c$ and $k = 0$ (vertical and slanted dashed lines) with the eigenmodes, pronouncing enhanced coupling phenomena and laterally propagated optical modes. (c) FDTD simulations exhibit optical coupling and the creation of lateral modes. Low coupling and photonic bandgap phenomena are observed for the hole size smaller than the half-wavelength. (d) Larger holes that are comparable to the wavelengths of the incident photons facilitate a higher number of optical modes and enhanced lateral propagation of light. (e) Calculated optical absorption in Si with a small hole ($d = 100$ nm, $p = 1000$ nm, and thickness, $t_{Si} = 1000$ nm) compared with the absorption of the large hole ($d = 700$ nm, $p = 1000$ nm, and thickness $= 1000$ nm). (f) For frequencies (period of holes/light wavelength) between 1.3 and 1.6, the normalized light group velocity (red curve) for 850 nm wavelength is significantly lower in photon-trapping Si compared to that of the bulk Si (blue line). The red curve represents an averaged group velocity for Si photon-trapping structures, which exhibits a distinctly lower value in our fabricated devices (Video 3, mp4, 12.4 MB [URL: https://doi.org/10.1117/1.APN.2.5.056001.s3]).

of p/λ, where p/λ is larger than unity. Figures 4(a) and 4(b) illustrate the relationship between lateral wave vector k and the incident wavelength for a hole size of 100 and 700 nm, respectively, under TE and TM polarizations. The solid curves represent the solutions for ΓX and ΓM directions, whereas the dots represent the areas between those directions, which are also provided in Fig. S14 in the Supplementary Material. First, a high-absorption characteristic can be observed under both TM and TE light incidences, as seen in the band diagram [Figs. 4(a) and 4(b)] and the comparative absorption curves provided in Fig. S15 in the Supplementary Material. It is noticeable that the larger holes pronounce curves with a smaller slope, which corresponds to a smaller group velocity. The next question is the coupling into the array. When significant lateral field

components are generated in the cylindrical coordinates for a hole with a specific dimension, the solutions of the wave vectors using Bessel functions can be given as $k_0 = 2\pi/\lambda$, $q_1^2 = k_0^2 - \beta^2$, and $q_2^2 = \varepsilon k_0^2 - \beta^2$, where k_0 is the wave vector for a given frequency in the vacuum, ε is the dielectric constant of Si, and β is the propagation constant. When the solution to the Bessel function q_2 is k_c, the lateral wave vectors are coupled with eigenmodes. The cross of the solution $k = k_c$ or $k = 0$ with the eigenmodes pronounces the modes that propagate laterally and can be absorbed in the material. It should be noted that the Bessel function was solved for a single hole, and it is expected that a similar characteristic can be achieved for an array of holes. For the small holes, we have the solutions only for the finite number of the eigenmodes with $k = 0$, which corresponds to the guided modes in photonic crystals. Such structures exhibit sharp spikes in absorption, as shown in Fig. 4(e). However, a continuous solution can be found in the large holey structures for the wavelengths ranging from 800 to 1000 nm, leading to a distinctly higher light absorption than in small holes, as depicted in Fig. 4(e). Hence, the optimized larger holey structures exhibit a good coupling phenomenon due to the relationship between the k vector and the eigenmodes.

In the next step, the influence of the size of the holes on the formation of lateral optical modes and the corresponding field distribution is studied. Coupling phenomena are only observed in the photon-trapping structures, as presented in Fig. S16 in the Supplementary Material. Low-coupling phenomena are observed for the devices with hole sizes smaller than half the wavelength, as shown in Fig. 4(c), where photons cannot efficiently couple within the absorber layer. However, for the hole size comparable with the incident wavelength, the light can couple into the holes and leak out through the sides of the hole, as illustrated in Fig. 4(d). The incident photons also reflect from the surface of photodetectors when the hole diameter is smaller than the incident wavelength, which is not the case for our most efficient fabricated devices. The hole diameters of our most optimized fabricated devices are comparable to the incident wavelength, similar to the one shown in Fig. 4(d). In photodetectors with larger holes, photons accumulate in the $x - z$ plane around the hole after coupling into laterally propagating modes and eventually getting absorbed there. Furthermore, the vertically illuminated light refracts at atan(n) angle from the boundary conditions, increasing light absorption in the active layer. Finally, the oxide layer of the SOI wafer underneath the sensors further contributes to enhanced photon absorption by reflecting the photons in the direction of the device surface. The influence of coupling for smaller and bigger holes at different incident angles is also studied on the photon absorption, as provided in Fig. S5 in the Supplementary Material. Photodetectors with larger holes ($d/p \sim 0.77$) exhibit noticeably higher light absorption, irrespective of incident angles, than devices with smaller holes. However, when illuminated with photons of longer wavelengths, a relatively higher photon absorption is obtained for the incident angle of 30 deg compared with 0 deg in both small and larger holes.

Slow light with reduced group velocity increases absorption efficiency due to the augmented light–matter interactions. The group velocity was calculated from the band diagram as $u_g = d\omega/dk$ under TE polarization modes, as presented in Fig. 4(f). The group velocity in bulk Si was calculated as c/n, where c is the light velocity and n is the refractive index of Si at 850 nm. The normalized frequency of our experimental structures is between 1.3 and 1.6. Herein, the group velocity in most modes for the normalized frequency between 1.3 and 1.6 is significantly lower than the group velocity of light in bulk Si. The average group velocity for the modes was also calculated, as shown by the red line, indicating a conspicuously lower average group velocity of the photon trapping structures compared to that of Si without such surface structures. Light-trapping surface structures have been demonstrated to be capable of enabling enhanced optical DOS with light enhancement beyond the ray optic limit.[58,59] Herein, the DOS was also calculated as an integral over the wave vector for a given frequency, $\rho(\omega) = \int\{\frac{d^d k}{(2\pi)^d}\}\delta[E - E(k)]$, in which d and E are differential dimension and energy, respectively. For the 2D photonic crystals, DOS could be approximated as $\rho_{2D}(\omega) = \frac{4\epsilon\omega}{\pi c^2}$.[27] The DOS of the photon-trapping photo detectors is found to be higher than that of the photodetectors with planar surfaces, as provided in Fig. S13(a) in the Supplementary Material. The photodetectors with micro-hole periods shorter than the incident wavelengths exhibit noticeably low DOS compared to the periods comparable to and slightly longer than the wavelengths. Our designed and fabricated photodetectors closely match with the shaded area on the right half of Fig. S13(a) in the Supplementary Material, exhibiting high DOS for frequencies higher than 1.0 (periods are comparable to or slightly longer than the incident wavelengths). Nevertheless, the region with high values of p/λ needs more Fourier components, and the maximum peaks of the DOS are not as pronounced as expected, while there is a constant increase of the optical mode density with p/λ. We conclude that observed absorption enhancement in Si is a combined effect of slow light with reduced group velocity, the enhanced photonic DOS, lateral propagation of a large number of optical modes, and efficient coupling of incident photons to the photon-trapping structures integrated on the Si surface. The cumulative impacts of the aforementioned processes help Si enhance light absorption by more than 20-fold and exceed the intrinsic absorption limit of GaAs.

We used a 1-μm thin Si film with photon-trapping structures to demonstrate ultrafast time response characteristics of ~31 ps full-width at half-maximum (FWHM) and 16 ps deconvolved time response at 850 nm, as shown in Fig. S13(b) in the Supplementary Material. Such ultrafast time response coupled with broadband very high-absorption efficiency exhibited by ultrathin Si helps overcome the bandwidth-absorption tradeoff faced by the ultrafast photodetector community. This work, thus, is very relevant to the design and fabrication of extremely fast and highly sensitive integrated photodetectors using modern CMOS foundry processes that currently use ultrathin Si of similar thickness.

6 Conclusions

We presented an experimental demonstration of photoabsorption enhancement by more than 20× in Si that effectively exceeds the intrinsic absorption limit of GaAs for a broad wavelength spectrum between 800 and 905 nm. In our demonstration, we used photodetectors designed with a 1 μm thin Si film integrated with an array of periodic photon-trapping structures that allow the generation of slow light with reduced group velocity, enhanced photon DOS, and, consequently, very high density of laterally propagating slow and stationary optical modes. This results in a more prolonged light–matter interaction time within the thin absorption region of the device. Intriguingly, simulated performances for ultrathin silicon

photodetectors with even thinner absorption regions, such as 30 and 100 nm thin films, exhibit similarly enhanced photosensitivity. Additionally, Si photon-trapping structures help reduce photodetectors' capacitance compared to their planar counterpart, enabling faster response. The fabrication process is CMOS-compatible and can contribute to integrated photodetectors with ultrafast responses for quantum computing, data communication systems, emerging biomedical imaging applications, biosensing, and autonomous vehicles.

Acknowledgments

We would like to thank Eli Yablonovitch for valuable discussions and H. Cansizoglu and Y. Gao for their help with the device fabrication. This work was supported in part by the US Army's Night Vision and Electronic Sensors Directorate (Grant No. W909MY-12-D-0008), NSF ECCS (Grant No. 1428392), and the S. P. Wang and S. Y. Wang Partnership, Los Altos, California (CA). Cesar Bartolo-Perez would like to acknowledge the National Council of Science and Technology and UC-MEXUS for the doctoral fellowship. Part of this study was carried out at the UC Davis Center for Nano and Micro Manufacturing.

References

1. T. Mueller, F. Xia, and P. Avouris, "Graphene photodetectors for high-speed optical communications," *Nat. Photonics* **4**, 297–301 (2010).
2. R. H. Hadfield, "Single-photon detectors for optical quantum information applications," *Nat. Photonics* **3**, 696–705 (2009).
3. H. Wang et al., "Optical interconnection networks for high-performance computing systems," *Rep. Prog. Phys.* **75**, 046402 (2012).
4. J. I. J. Wang et al., "Hexagonal boron nitride as a low-loss dielectric for superconducting quantum circuits and qubits," *Nat. Mater.* **21**, 398–403 (2022).
5. R. M. C. Andrade et al., "What changes from ubiquitous computing to internet of things in interaction evaluation?" *Lect. Notes Comput. Sci.* **10291**, 3–21 (2017).
6. B. Xu et al., "Ubiquitous data accessing method in IoT-based information system for emergency medical services," *IEEE Trans. Ind. Inf.* **10**, 1578–1586 (2014).
7. A. Kirmani et al., "First-photon imaging," *Science.* **343**, 58–61 (2014).
8. G. Allen and T. Chan, *Artificial Intelligence and National Security*, Harvard Kennedy School (2017).
9. G. A. Kaissis et al., "Secure, privacy-preserving and federated machine learning in medical imaging," *Nat. Mach. Intell.* **2**, 305–311 (2020).
10. X. Michalet et al., "Development of new photon-counting detectors for single-molecule fluorescence microscopy," *Philos. Trans. R. Soc. B Biol. Sci.* **368**, 20120035 (2013).
11. J. Unger et al., "Real-time diagnosis and visualization of tumor margins in excised breast specimens using fluorescence lifetime imaging and machine learning," *Biomed. Opt. Express* **11**, 1216–1230 (2020).
12. Y. Sun et al., "Intraoperative visualization of the tumor microenvironment and quantification of extracellular vesicles by label-free nonlinear imaging," *Sci. Adv.* **4**, eaau5603 (2018).
13. A. Dargys and J. Kundrotas, *Handbook on Physical Properties of Ge, Si, GaAs and InP*, Science and Encyclopedia Publishers (1994).
14. C. Schinke et al., "Uncertainty analysis for the coefficient of band-to-band absorption of crystalline silicon," *AIP Adv.* **5**, 067168 (2015).
15. T. Tiedje et al., "Limiting efficiency of silicon solar cells," *IEEE Trans. Electron Devices* **31**, 711–716 (1984).
16. P. Y. Yu and M. Cardona, *Fundamentals of Semiconductors*, Springer (1999).
17. Z. Zhou, B. Yin, and J. Michel, "On-chip light sources for silicon photonics," *Light Sci. Appl.* **4**, e358 (2015).
18. M. Veldhorst et al., "Silicon CMOS architecture for a spin-based quantum computer," *Nat. Commun.* **8**, 1–8 (2017).
19. E. Yablonovitch and G. D. Cody, "Intensity enhancement in textured optical sheets for solar cells," *IEEE Trans. Electron Devices* **29**, 300–305 (1982).
20. E. Garnett and P. Yang, "Light trapping in silicon nanowire solar cells," *Nano Lett.* **10**, 1082–1087 (2010).
21. A. Ingenito, O. Isabella, and M. Zeman, "Experimental demonstration of $4n^2$ classical absorption limit in nanotextured ultrathin solar cells with dielectric omnidirectional back reflector," *ACS Photonics* **1**, 270–278 (2014).
22. I. Schnitzer et al., "30% external quantum efficiency from surface textured, thin-film light-emitting diodes," *Appl. Phys. Lett.* **63**, 2174 (1998).
23. T. Tiedje et al., "Photoconductivity enhancement by light trapping in rough amorphous silicon," *Appl. Phys. Lett.* **42**, 712 (1998).
24. S. Manzoor et al., "Visualizing light trapping within textured silicon solar cells," *J. Appl. Phys.* **127**, 063104 (2020).
25. S. B. Mallick, M. Agrawal, and P. Peumans, "Optimal light trapping in ultra-thin photonic crystal crystalline silicon solar cells," *Opt. Express* **18**, 5691–5706 (2010).
26. N. Afifah Yahaya et al., "Characterization of light absorption in thin-film silicon with periodic nanohole arrays," *Opt. Express* **21**, 5924–5930 (2013).
27. K. X. Wang et al., "Light trapping in photonic crystals," *Energy Environ. Sci.* **7**, 2725–2738 (2014).
28. Z. Yu, A. Raman, and S. Fan, "Fundamental limit of nanophotonic light trapping in solar cells," *Proc. Natl. Acad. Sci. U. S. A.* **107**, 17491–17496 (2010).
29. J. M. Gee, "Optically enhanced absorption in thin silicon layers using photonic crystals," in *Conf. Rec. IEEE Photovolt. Spec. Conf.*, pp. 150–153 (2002).
30. A. A. Asatryan et al., "Mode-based analysis of silicon nanohole arrays for photovoltaic applications," *Opt. Express*, **22**, A1343–A1354 (2014).
31. P. Bermel et al., "Improving thin-film crystalline silicon solar cell efficiencies with photonic crystals," *Opt. Express* **15**, 16986–17000 (2007).
32. D. Zhou and R. Biswas, "Photonic crystal enhanced light-trapping in thin film solar cells," *J. Appl. Phys.* **103**, 093102 (2008).
33. D. Pacifici et al., "How much can guided modes enhance absorption in thin solar cells?" *Opt. Express* **17**, 20975–20990 (2009).
34. S. Pillai et al., "Surface plasmon enhanced silicon solar cells," *J. Appl. Phys.* **101**, 093105 (2007).
35. T. Ishi et al., "Si nano-photodiode with a surface plasmon antenna," *Jpn. J. Appl. Phys.* **44**, L364 (2005).
36. D. Madzharov, R. Dewan, and D. Knipp, "Influence of front and back grating on light trapping in microcrystalline thin-film silicon solar cells," *Opt. Express* **19**, A95 (2011).
37. R. Bergmann et al., "Optimal light trapping in ultra-thin photonic crystal crystalline silicon solar cells," *Opt. Express* **18**, 5691–5706 (2010).
38. S. Bhattacharya and S. John, "Beyond 30% conversion efficiency in silicon solar cells: a numerical demonstration," *Sci. Rep.* **9**, 1–15 (2019).
39. K. Yoshikawa et al., "Exceeding conversion efficiency of 26% by heterojunction interdigitated back contact solar cell with thin film Si technology," *Sol. Energy Mater. Sol. Cells* **173**, 37–42 (2017).
40. J. Dréon et al., "23.5%-efficient silicon heterojunction silicon solar cell using molybdenum oxide as hole-selective contact," *Nano Energy* **70**, 104495 (2020).
41. A. K. Katiyar et al., "Breaking the absorption limit of Si toward SWIR wavelength range via strain engineering," *Sci. Adv.* **6**, 576–605 (2020).

42. G. Konstantatos and E. H. Sargent, "Nanostructured materials for photon detection," *Nat. Nanotechnol.* **5**, 391–400 (2010).
43. E. Özbay et al., "Fabrication of high-speed resonant cavity enhanced Schottky photodiodes," *IEEE Photonics Technol. Lett.* **9**, 672–674 (1997).
44. W. K. Huang, Y. C. Liu, and Y. M. Hsin, "A high-speed and high-responsivity photodiode in standard CMOS technology," *IEEE Photonics Technol. Lett.* **19**, 197–199 (2007).
45. Y. Gao et al., "Photon-trapping microstructures enable high-speed high-efficiency silicon photodiodes," *Nat. Photonics* **11**, 301–308 (2017).
46. H. Cansizoglu et al., "A new paradigm in high-speed and high-efficiency silicon photodiodes for communication. — Part I. Enhancing photon-material interactions via low-dimensional structures," *IEEE Trans. Electron Devices* **65**(2), 372–381 (2018).
47. H. Cansizoglu et al., "Dramatically enhanced efficiency in ultra-fast silicon MSM photodiodes via light trapping structures," *IEEE Photonics Technol. Lett.* **31**, 1619–1622 (2019).
48. K. Zang et al., "Silicon single-photon avalanche diodes with nano-structured light trapping," *Nat. Commun.* **8**, 1–6 (2017).
49. D. Chen et al., "Photon-trapping-enhanced avalanche photodiodes for mid-infrared applications," *Nat. Photonics* **17**, 594–600 (2023).
50. M. L. Hsieh et al., "Experimental demonstration of broadband solar absorption beyond the Lambertian limit in certain thin silicon photonic crystals," *Sci. Rep.* **10**, 11857 (2020).
51. C. Bartolo-Perez et al., "Maximizing absorption in photon-trapping ultrafast silicon photodetectors," *Adv. Photonics Res.* **2**, 2000190 (2021).
52. S. Salahuddin, K. Ni, and S. Datta, "The era of hyper-scaling in electronics," *Nat. Electron.* **1**, 442–450 (2018).
53. R. Maurand et al., "A CMOS silicon spin qubit," *Nat. Commun.* **7**, 1–6 (2016).
54. T. G. Mayerhöfer, S. Pahlow, and J. Popp, "The Bouguer–Beer–Lambert law: shining light on the obscure," *ChemPhysChem* **21**, 2029–2046 (2020).
55. A. Beer, *Grundriss des photometrischen Calcüles*, Bayerische Staatsbibliothek, München (1854).
56. S. Adachi, "Optical dispersion relations for GaP, GaAs, GaSb, InP, InAs, InSb, $Al_xGa_{1-x}As$, and $In_{1-x}Ga_xAs_yP_{1-y}$," *J. Appl. Phys.* **66**, 6030 (1998).
57. E. D. Palik, *Handbook of Optical Constants of Solids*, Vol. **1**, pp. xvii–xviii, Elsevier (1985).
58. S. Mokkapati and K. R. Catchpole, "Nanophotonic light trapping in solar cells," *J. Appl. Phys.* **112**, 101101 (2012).
59. D. M. Callahan, J. N. Munday, and H. A. Atwater, "Solar cell light trapping beyond the ray optic limit," *Nano Lett.* **12**, 214–218 (2012).
60. S. Radovanović, A. J. Annema, and B. Nauta, "A 3-Gb/s optical detector in standard CMOS for 850-nm optical communication," *IEEE J. Solid-State Circuits* **40**, 1706–1717 (2005).
61. M. K. Emsley, O. Dosunmu, and M. S. Ünlü, "High-speed resonant-cavity-enhanced silicon photodetectors on reflecting silicon-on-insulator substrates," *IEEE Photonics Technol. Lett.* **14**, 519–521 (2002).
62. M. S. Ünlü et al., "High-speed Si resonant cavity enhanced photodetectors and arrays," *J. Vac. Sci. Technol. A* **22**, 781 (2004).
63. R. T. Chen et al., "Fully embedded board-level guided-wave optoelectronic interconnects," *Proc. IEEE* **88**, 780–793 (2000).
64. H. Shigeta et al., "Enhancement of photocurrent in ultrathin active-layer photodetecting devices with photonic crystals," *Appl. Phys. Lett.* **101**, 161103 (2012).
65. B. Yang et al., "10-Gb/s all-silicon optical receiver," *IEEE Photonics Technol. Lett.* **15**, 745–747 (2003).
66. R. Swoboda and H. Zimmermann, "11 Gb/s monolithically integrated silicon optical receiver for 850nm wavelength," in *Dig. Tech. Pap. - IEEE Int. Solid-State Circuits Conf.* (2006).
67. S. Radovanovic et al., "An integrated 12.5-Gb/s optoelectronic receiver with a silicon avalanche photodetector in standard SiGe BiCMOS technology," *Opt. Express* **20**, 28153–28162 (2012).
68. S. M. Csutak et al., "Integrated silicon optical receiver with avalanche photodiode," *IEE Proc. Optoelectron.* **150**, 235–237 (2003).
69. M. Atef, A. Polzer, and H. Zimmermann, "Avalanche double photodiode in 40-nm standard CMOS technology," *IEEE J. Quantum Electron.* **49**, 350–356 (2013).
70. M.-J. Lee et al., "A fully-integrated 12.5-Gb/s 850-nm CMOS optical receiver based on a spatially-modulated avalanche photodetector," *Opt. Express* **22**, 2511–2518 (2014).
71. J. S. Youn et al., "10-Gb/s 850-nm CMOS OEIC receiver with a silicon avalanche photodetector," *IEEE J. Quantum Electron.* **48**, 229–236 (2012).
72. M.-J. Lee et al., "A silicon avalanche photodetector fabricated with standard CMOS technology with over 1 THz gain-bandwidth product," *Opt. Express* **18**, 24189–24194 (2010).
73. A. C. Ulku et al., "A 512 × 512 SPAD image sensor with integrated gating for widefield FLIM," *IEEE J. Sel. Top. Quantum Electron.* **25**, 6801212 (2019).
74. D. Stoppa et al., "Single-photon avalanche diode CMOS sensor for time-resolved fluorescence measurements," *IEEE Sens. J.* **9**, 1084–1090 (2009).
75. C. Li et al., "Grating-enabled high-speed high-efficiency surface-illuminated silicon photodiodes," *Opt. Express* **29**, 3458–3464 (2021).
76. B. Wang et al., "A low-voltage Si-Ge avalanche photodiode for high-speed and energy efficient silicon photonic links," *J. Light. Technol.* **38**, 3156–3163 (2020).
77. T. Li et al., "Spatially controlled electrostatic doping in graphene p-i-n junction for hybrid silicon photodiode," *NPJ 2D Mater. Appl.* **2**, 1–8 (2018).

Wayesh Qarony, a postdoctoral scholar at the University of California Berkeley in the EECS Department, works jointly with the LBNL. He focuses on nanophotonic design, fabrication, and characterization of optoelectronic, photonics, and quantum semiconductor devices. He received his PhD in applied physics and MSc in electrical engineering from Hong Kong Polytechnic University and Jacobs University Bremen, Germany, respectively. Before joining UC Berkeley & LBNL, he was a postdoctoral scholar at ECE UC Davis.

Ahmed S. Mayet received his MS in electrical and computer engineering from the University of California, Davis, in 2017 and PhD in electrical and computer engineering with emphasis in biophotonics and bioimaging from the University of California, Davis, in 2023. His research focused on developing ultra-fast and efficient optoelectronic devices for ultra-fast optical communication, biomedical imaging, and NIR imaging and sensing. He joined Taibah University, Saudi Arabia, in 2023, where he is currently an assistant professor.

Ekaterina Ponizovskaya Devine received the MS and PhD degrees from the Moscow Institute of Physics and Technology (State University), Moscow, Russia, in 1999. She was with the Ames Center, NASA, Mountain View, CA, United States, where she was involved in the optimization and physics-based models for prognostics and automation. She is currently with W&WSens Device, Inc., Los Altos, CA, United States, where she is focusing on photonics and photodetectors.

Soroush Ghandiparsi received the BSc degree in electrical engineering and the MSc degree in nanophotonic engineering from the School of Engineering Emerging Technology, Sharif University of Technology, Tehran, Iran, in 2009 and 2012, respectively. He received PhD in electrical engineering with emphasis in biophotonics and bioimaging from the University of California, Davis. Currently, his research is focused on developing a novel high-speed and efficient Silicon-based photodetector

integrated with transimpedance amplifier (TIA)/equalizer analog circuits in the photonic BiCMOS platform.

Cesar Bartolo-Perez graduated from the University of California, Davis, with a PhD in electrical and computer engineering. His research focused on the development of single-photon avalanche photodetectors for lidar and biomedical applications. He is currently developing silicon photonic integrated systems for the same applications. He also holds an MSc from the National Institute of Astrophysics, Optics and Electronics, Mexico, and a BSc in technology from the National University Autonomous of Mexico.

Ahasan Ahamed is a second-year graduate student pursuing his PhD in the Electrical and Electronics Engineering Department at the University of California, Davis. He received a BSc degree from Bangladesh University of Engineering and Technology in 2018. He is currently working on spectral response engineering of photontrapping photodiodes paving towards spectrometer-on-a-chip. His research also include designing ultra-fast photodiodes and SPADs for hyperspectral imaging.

Amita Rawat received her BTech degree in electrical engineering from IIT Patna, India, and her PhD in microelectronics (logic device variability modeling and device fabrication) from the Department of Electrical Engineering IIT Bombay. She worked in IMEC Leuven, Belgium, on compact modeling of advance logic transistors. She is currently working as a postdoctoral fellow at University of California, Davis, on optoelectronic device modeling, simulation, and fabrication.

Hasina H. Mamtaz received the BS in environmental engineering in 1995, from Middle East Technical University, Ankara, Turkey, and MS degree in computer engineering from California State University at Long Beach. She worked for Gazillion Bits, Inc., San Jose, CA, and W&WSens Devices, Inc., Los Altos, CA. Currently, she is a program manager at UC Davis.

Toshishige Yamada received the BS and MS degrees in physics from the University of Tokyo, Japan, and the PhD in electrical engineering from Arizona State University. Following a postdoctoral fellow in applied physics at Stanford University, he joined the NASA Ames Research Center, and Santa Clara University, CA. He is currently an adjunct professor at the UC Santa Cruz and studies the theory and simulations of advanced semiconductor materials and devices.

Shih-Yuan Wang received a BS engineering physics in 1969, from UC Berkeley; and PhD in electrical engineering and computer sciences, in 1977 from UC Berkeley. At HP Labs, SY worked on multimode vertical cavity surface emitting lasers and high speed III-V photodiodes, both of which became successful products. He is currently with W&WSens Devices, Inc. Los Altos, CA, working on silicon photodiodes compatible with CMOS process for CMOS image sensors, optical interconnects, and lidar applications.

M. Saif Islam received a BSc degree in physics from Middle East Technical University, Ankara, in 1994, an MS degree in physics from Bilkent University, Ankara, in 1996, and the PhD in electrical engineering from UCLA, in 2001. He joined the University of California, Davis, in 2004, where he is currently a professor. He is a fellow of AAAS, Optica, SPIE, IEEE, and the National Academy of Inventors.

Supplementary Materials for

Achieving higher photoabsorption than group III-V semiconductors in ultra-fast thin silicon photodetectors with integrated photon-trapping surface structures

Wayesh Qarony[1†], Ahmed S. Mayet[1†], Ekaterina Ponizovskaya Devine[2], Soroush Ghandiparsi[1], Cesar Bartolo-Perez[1], Ahasan Ahamed[1], Amita Rawat[1], Hasina H. Mamtaz[1], Toshishige Yamada[2,3], Shih-Yuan Wang[2], M. Saif Islam[1*]

[1]Electrical and Computer Engineering, University of California—Davis; Davis, CA 95618, USA.
[2]W&WSens Devices, Inc., 4546 El Camino; Los Altos, CA 94022, USA.
[3]Electrical and Computer Engineering, Baskin School of Engineering; University of California, Santa Cruz, CA 95064, USA.

[†] These authors contributed equally to this work
[*]Corresponding author. Email: sislam@ucdavis.edu

This PDF file includes:

Supplementary Text
Figs. S1 to S11
Tables S1
Captions for Movies S1 to S3
References

Other Supplementary Materials for this manuscript include the following:

Movies S1 to S3

1 Fabrication of photodetectors

The Si absorber layer (*p*-type) with a thickness of 1000 nm was epitaxially grown on a silicon-on-insulator (SOI) substrate. The SOI wafer has a 1000 nm buried oxide layer BOX, where the active layer was epitaxially grown with a resistivity of 14-22 ohm-cm. Next, the native oxide was removed by cleaning the surface of the Si with buffered oxide etching BOE (6:1) process. The fabrication process flow chart is shown in Fig. S1, while the detailed process steps are described in the following.

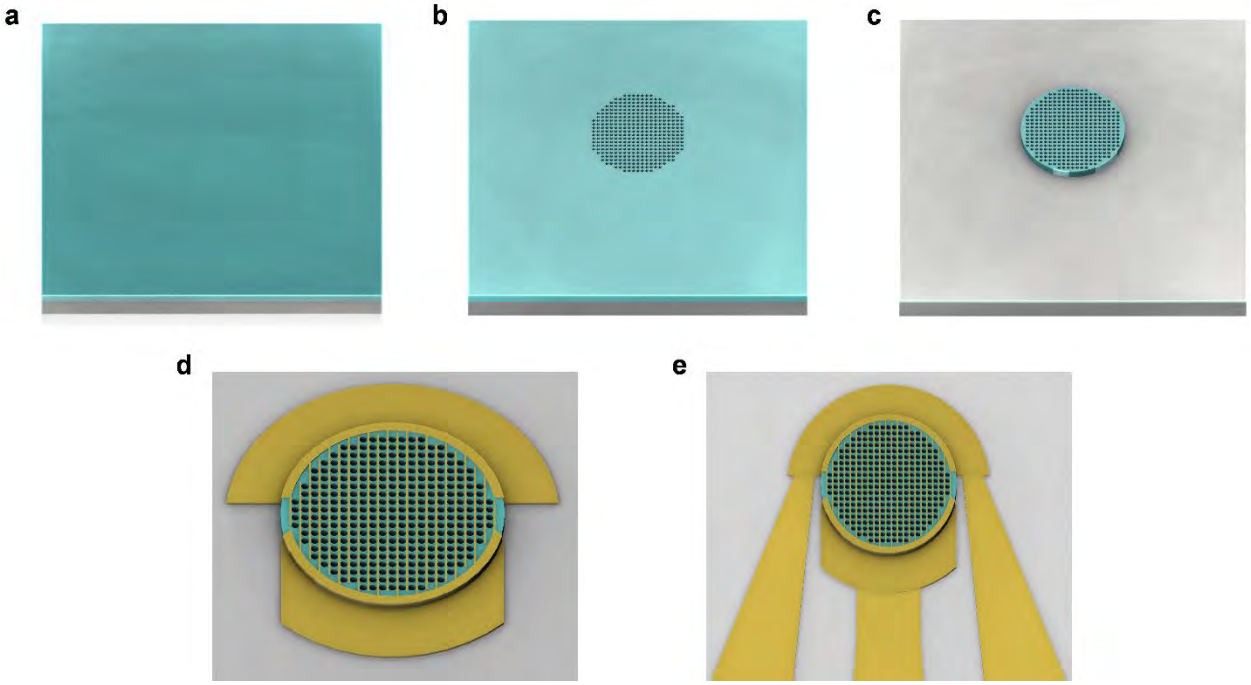

Figure S1: **Flow chart of the fabrication process of Si metal-semiconductor-metal photon-trapping photodetectors devices.** (**a**) Epitaxially grown p-type 1000 nm thick silicon on SiO_2 SOI wafer. (SOI wafer substrate: Gray (SiO_2), epitaxially grown Si: Turquoise (Si)). The native oxide of the wafer is cleaned by the buffered oxide etching BOE (6:1) process. (**b**) Photon-trapping holes patterning using DUV photolithography and DRIE holes etching. (**c**) Mesa etches to the substrate layer (SiO_2). (**d**) 100 nm thick, and 300 nm width interdigitated aluminum (Al)

metals sputtered and lift-off to form Schottky contact: Gold (interdigitated Schottky contact). (**e**) Coplanar waveguide metal deposition (CPW: Gold).

1.1 Photon-trapping hole formation

Right after the wafer cleaning, sub-micron photon-trapping (PT) hole arrays were patterned using a stepper lithography system. In the stepper system, we can adjust the focus of the ultraviolet (UV) light to shrink the features present on the mask plate and enables sub-micron feature patterning. Next, PT hole arrays were etched in a reactive ion etching (RIE) process. Fluorine-based chemistry was utilized to etch holes in the silicon. The fabricated PT structures possess a period, diameter, and hole depth of 1300, 1000, and 600 nm, respectively.

1.2 Mesa isolation

In this process step, the top and the bottom mesa structures of the photodetector were patterned. The top mesa was defined followed by the bottom mesa in alignment with the previously patterned PT structures by utilizing the stepper and RIE system. Patterning the top mesa exposes the bottom contact layer on the stack, whereas the bottom mesa patterning isolates the photodetectors from the neighboring devices.

1.3 Metallization

In the next step, the Si substrate was cleaned with BOE (6:1) to remove the native oxide before the metal deposition. The interdigitated aluminum (Al) fingers with a thickness of 100 nm and width of 300 nm were sputtered on the Si in an RF sputter system. Uniform Schottky contacts were prepared by lifting off the sputtered Al.

1.4 Co-planner waveguide patterning

After the metallization, the sample was patterned for co-planar waveguide contact. In this step, about 300 nm of Al layer was deposited followed by a lift-off process to create coplanar waveguides (CPW), which utilizes for the high-speed transport of the electrical pulse converted from a picosecond (ps) pulsed laser by the fabricated photodetectors.

1.5 Passivation

The passivation process step is conducted after completing the fabrication of the devices. To passivate the surface states created on the sidewalls of the holes and mesa, 2% HF was used for 3 seconds with HF:H_2O, 1:100 ratio. The hydrogen ion present in the solution attaches itself to the surfaces and neutralizes the active surface state. This passivation process reduces the dark state leakage current.

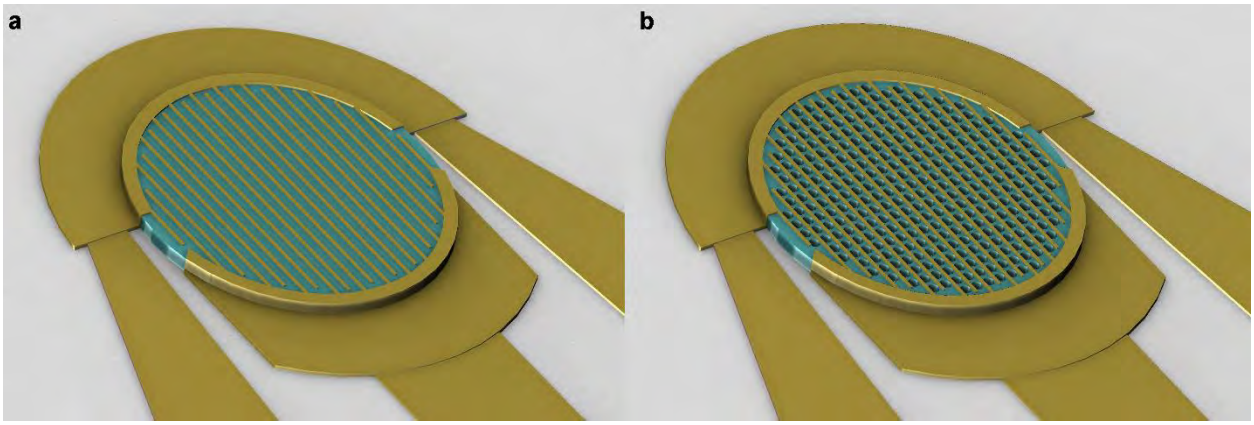

Figure S2: **Schematic of Si MSM fabricated photodetector devices.** (**a**) Planar (flat) surface**,** (**b**) Photon trapping Si MSM photodetector.

Metal semiconductor metal or MSM control photodetectors without integrated PT structures were also fabricated to compare their performance with the PT MSM photodetectors. The schematics of both control and PT photodetectors are shown in Fig. S2, while the optical

microscopy images of fabricated devices with various mesa sizes, photon trapping structures with holes diameters as well as periodicities are illustrated in Fig. S3.

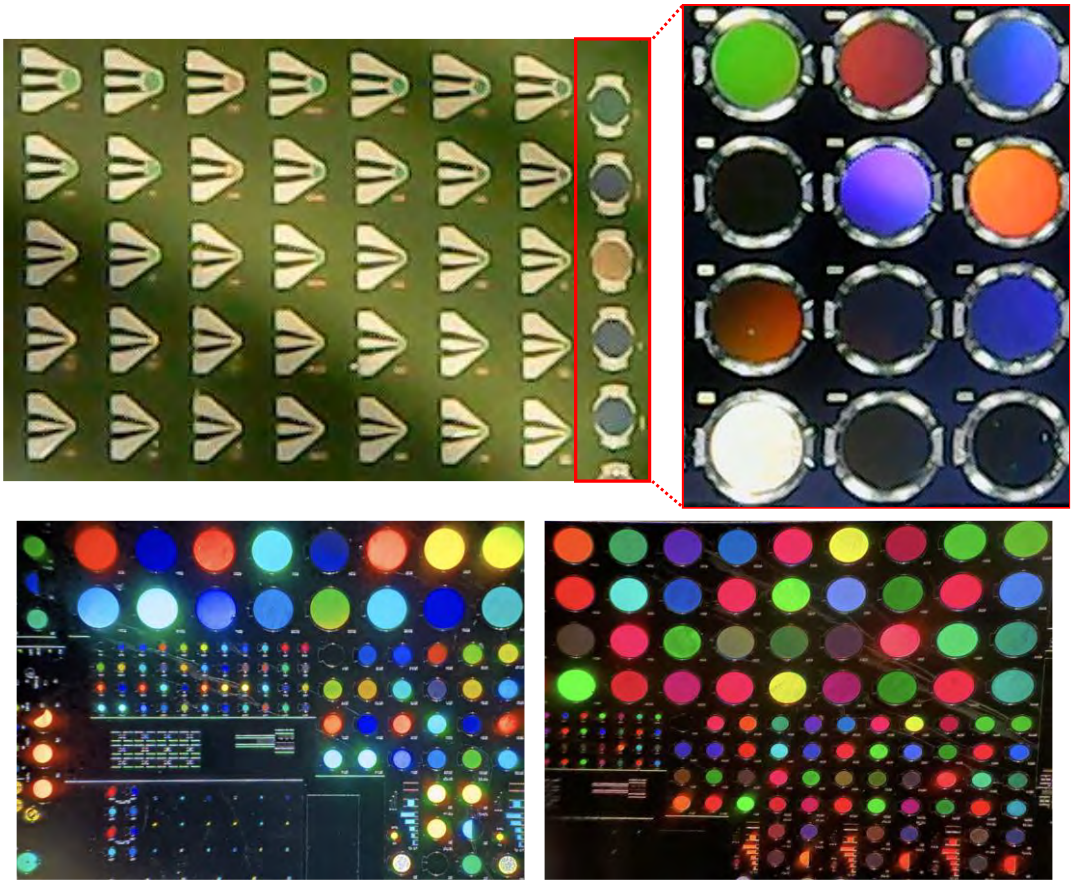

Figure S3: **Optical images of fabricated photodetectors.** Optical microscopy images of fabricated devices with various mesa sizes, different photon-trapping structures with varying hole diameters (*d*), and periodicities (*p*) (Left Top). The change in emission color from the surface of the devices indicates wavelength-dependent photosensitivity for varying device diameter, *d*, and *p* (All other images).

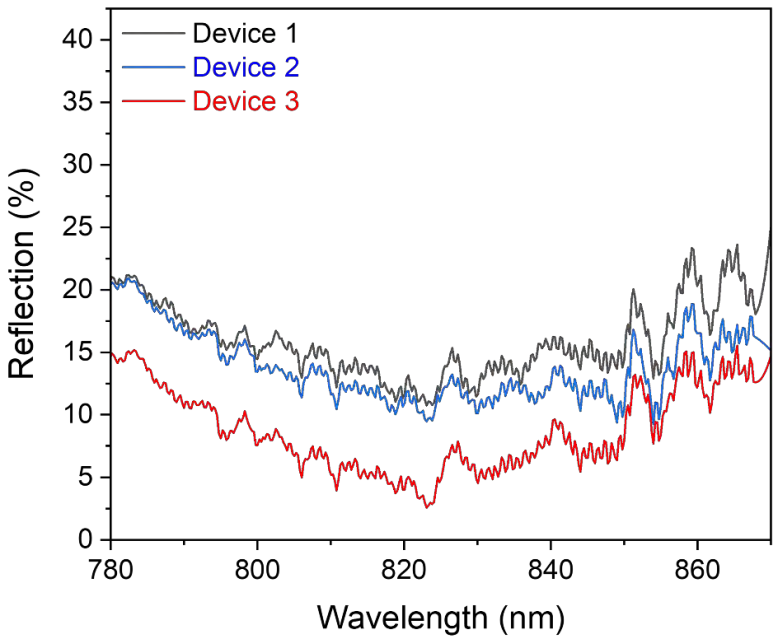

Figure S4: **Measured reflection characteristics of photon-trapping devices by varying the diameter and periodicity of holes.**

2. Simulation methods

A 3D finite-difference time-domain (FDTD) optical simulation was utilized to rigorously solve Maxwell's curl equations to calculate the electromagnetic (EM) fields within the photodetectors. The simulations were performed for the array of cylindrical holes of 700 nm diameter with a 1000 nm period in Si slab of 1000 nm thin on SiO_2 substrate. The depth of the holes was assumed to be 1000 nm. Furthermore, the optical absorption in Si was approximated by the Lorentz model with parameters fitted to the data at the range of around 850 nm wavelength. In FDTD, the incident pulse had a Gaussian-shaped spectrum between 600 to 1200 nm, spatially it is a plane wave. The averaged amplitude vs. wavelengths of the signal that were reflected and transmitted at the bottom and the sides were detected using Fourier transform. Then the reflected (R) and transmitted (T)

power normalized to the input source were calculated. The absorption (A) was calculated as $A = 1 - R - T$. Boundary conditions in the direction of light propagation were assumed to be Perfectly Matched Layers (PML). Periodical boundary conditions were considered for the other directions around the simulation area.

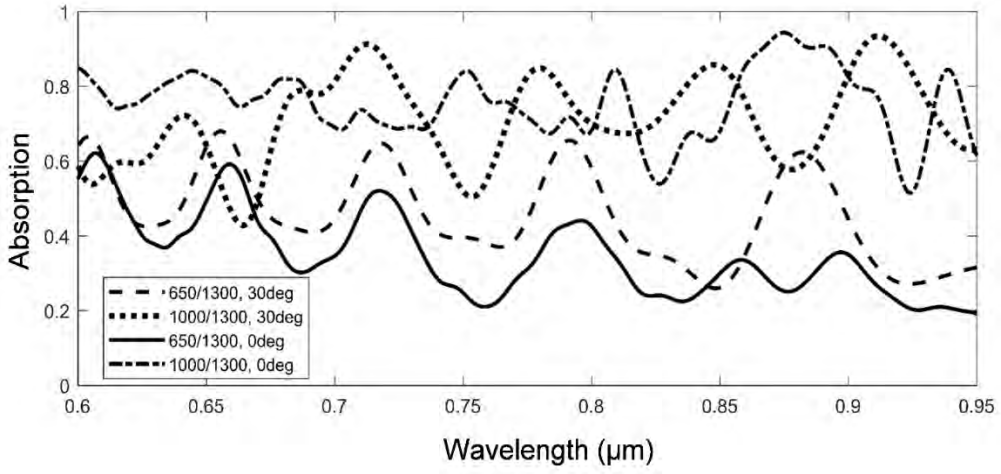

Figure S5: **Photon absorption in photodetectors with small and large holes under different illumination angles.** Effect of coupling phenomena for small and large holes at different incident angles of light on the photon absorption in Si photon-trapping photodetectors.

Fig. S6 estimates optical losses caused by the interdigitated metal on top of the MSM planar (Fig. S6(a)) and photon-trapping (Fig.S6(b)) photodetectors. The curves represent the plane wave normal to the surface for the E component of the EM field parallel to the metal fingers vs. the perpendicular and the averaged value. A very low absorption loss has been observed due to the interdigitated metal in photon-trapping devices compared to the planar devices.

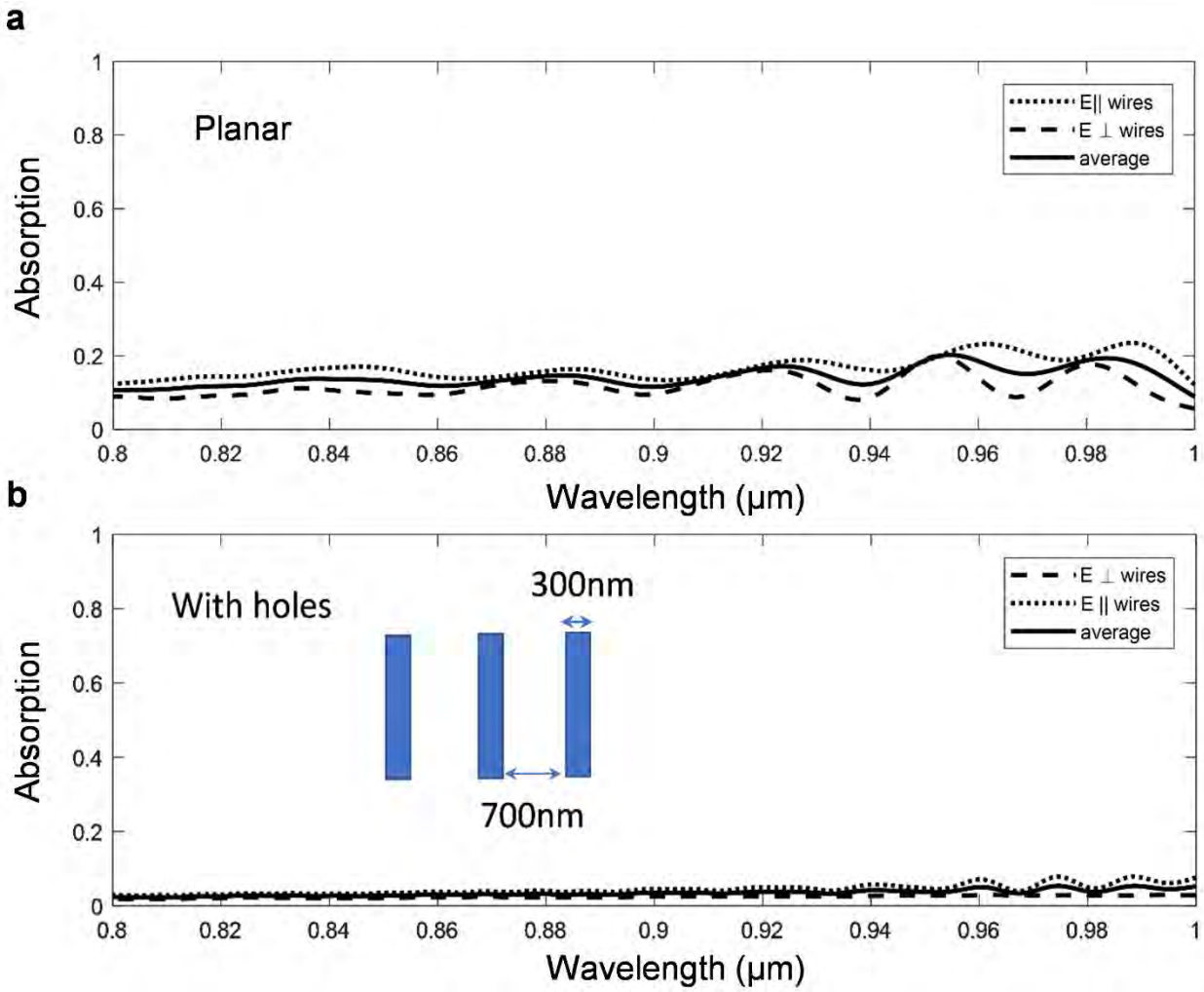

Figure S6**: Optical absorption of the aluminum interdigitated metals.** (**a**) Optical absorption of Al interdigitated metals in planar Si MSM photodetector, (**b**) Extremely low optical absorption of Al interdigitated metals in photon trapping Si MSM photodetectors.

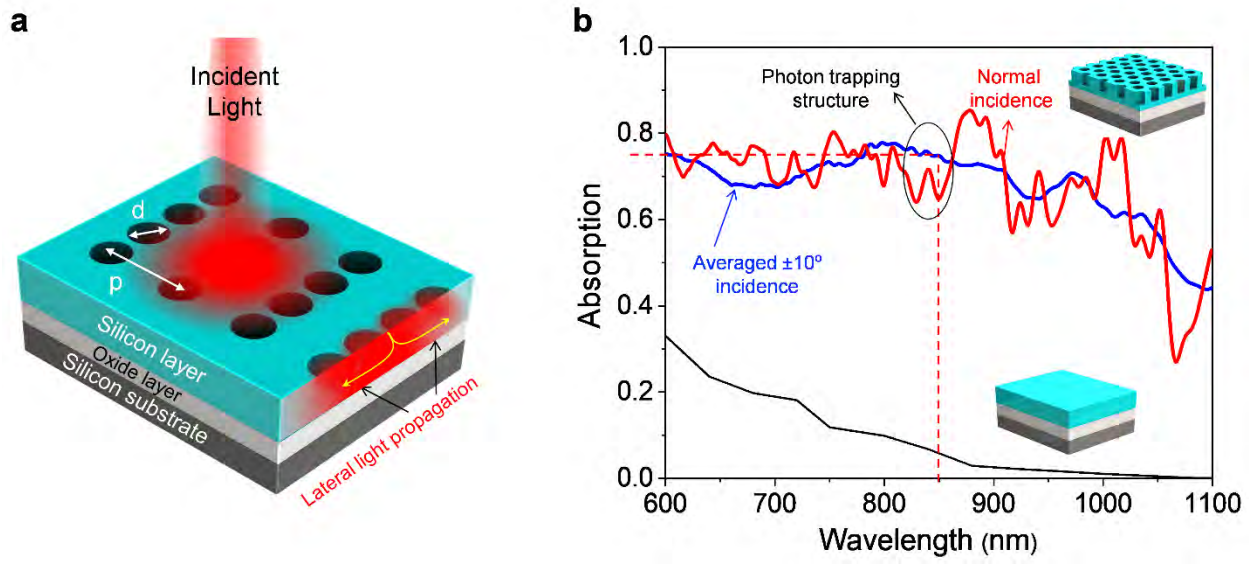

Figure S7: **Optical absorption in photon-trapping silicon photodetectors under normally incident illumination and incident light with different angles** (**a**) Schematic of silicon slab on silicon-on-insulator (SOI) integrated with cylindrical photon-trapping holes that allow lateral propagation of light resulting in enhanced optical path length and photon absorption, where (*p*) is the periodicity of the photon-trapping array, and (*d*) is the photon-trapping hole diameter, (**b**) A comparison of simulated absorption of photon-trapping and planar (flat) Si MSM photodetectors, where red and blue curves are simulated absorption spectra for normally incident light and averaged among ±10° angles, respectively.

The cross-sectional simulation structure is schematically shown in Fig. S6 (a). A thin Si absorber is assumed to be prepared on an SOI substrate. The photon-trapping photodetector is simulated for absorptions in wavelengths ranging from 600 nm to 1100 nm as presented in Fig. S6 (b). A photodetector with a planar surface is also simulated as a reference. The red and blue curves are simulated absorption spectra of photon-trapping photodetectors for normally incident light and incident light averaged between ±10° angles, respectively. The photon-trapping photodetectors exhibit distinctly higher absorption in comparison with the planar counterpart. For devices with

photon-trapping structures and the normally incident light illumination, a maximum photon absorption exceeding 85% is achieved around 880 nm wavelength. We also observe that the simulated devices exhibit photon absorption beyond $4n^2$ (n is the refractive index of the silicon material as a function of incident wavelength) in the wavelength spectrum ranging from 820 nm to 1100 nm as can be seen. Moreover, the maximum absorption enhancement can be as high as $27n^2$ by integrating our fabricated devices' most optimized photon-trapping holes. The corresponding calculated responsivities of the characterized devices are also depicted in Fig. S7 for a broad wavelength spectrum.

We have attached a numerical simulation showing the optical absorption in an optimized square lattice pattern with circular holes and compared it with a hexagonal lattice pattern with circular holes. Photon-trapping holes arranged in hexagonal lattice show higher optical coupling performance than the square lattice, as depicted in Fig. S8, since the incident light couples more efficiently in such a design, resulting in enhanced optical path length and light-matter interactions.

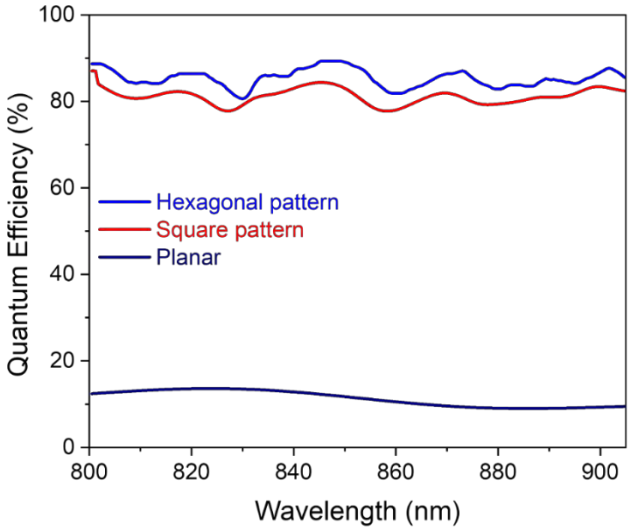

Figure S8: Comparison of calculated quantum efficiency between planar and photon-trapping silicon photodetectors with hexagonal and square patterns.

Then the influence of different microhole shapes/channels on the quantum efficiency of 1.0-micrometer thick silicon photon-trapping photodetectors has been studied, as presented in Fig. S9. It should be mentioned here that the simulations are performed based on a single micromole, and the devices are not optimized. The goal was to justify that different shapes would impact light-matter interaction differently.

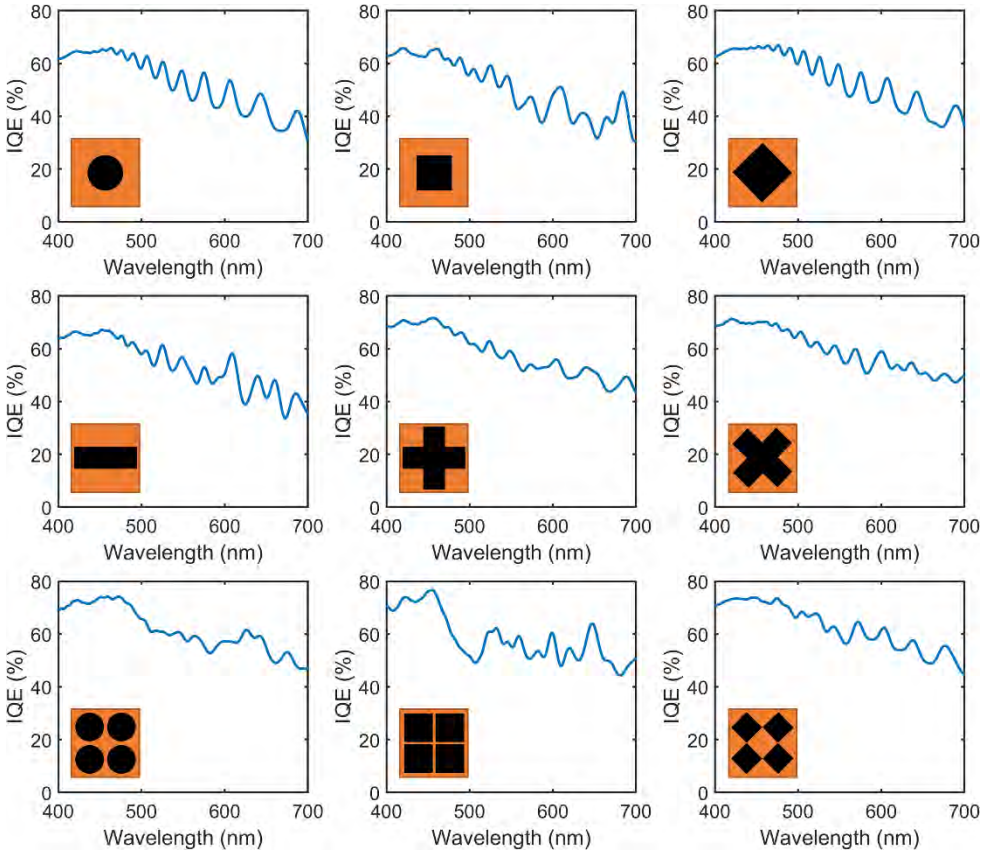

Figure S9: Comparison of calculated quantum efficiency with varying photon-trapping hole shapes. The devices are studied based on a single hole and are not optimized.

The measured dark current characteristics of a 50 µm planar and photon-trapping photodetectors are presented in Fig. S10. The planar device exhibits 67 nA dark current at 3V biasing, whereas the photon-trapping pronounces 157 nA.

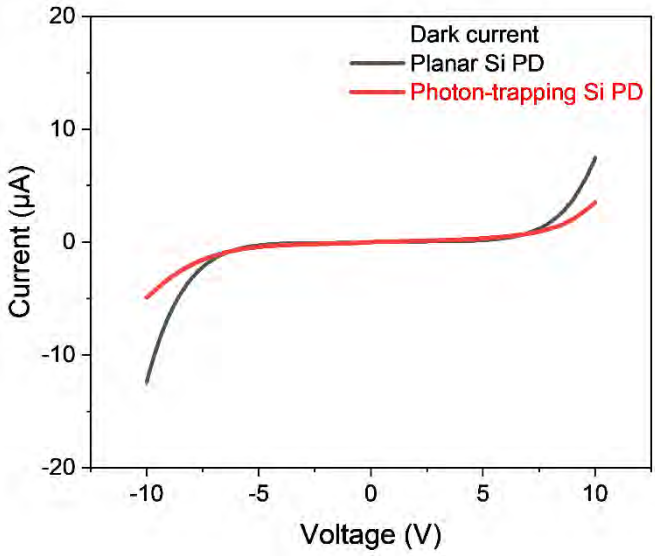

Figure S10: Dark current characteristics of the fabricated 50 µm planar and photon-trapping photodetectors.

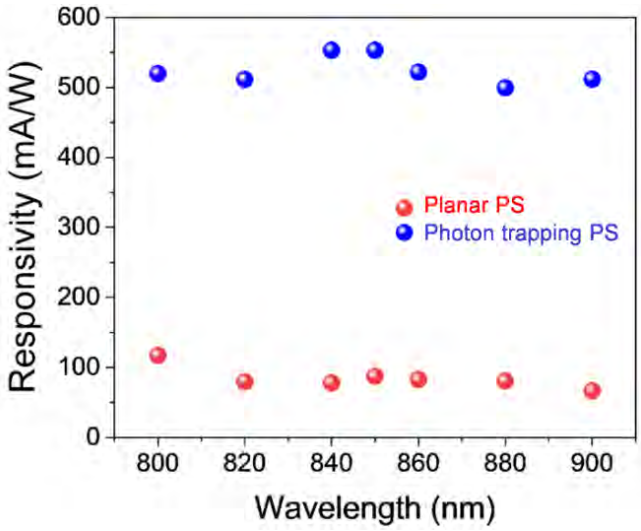

Figure S11: **Responsivity of the fabricated photodetectors.** The measured responsivity of the fabricated control and photon-trapping photodetectors. The periodicity (p) and diameter of the photon-trapping structures are 1300 and 1000 nm, respectively, while the device's active layer thickness (t_{Si}) is 1000 nm.

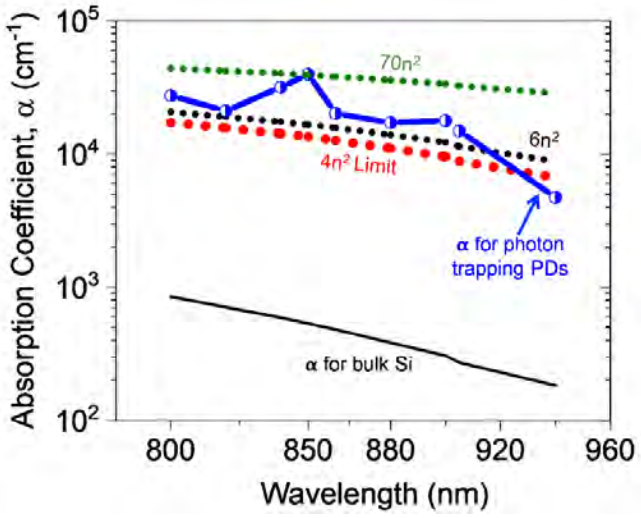

Figure S12: **Excellent enhanced absorption coefficient obtained from the fabricated photon-trapping photodetectors.** The maximum enhanced absorption coefficient obtained from the most optimized fabricated photon-trapping photodetectors exceeded $70n^2$, where n is the refractive

index of the material. The devices were measured by a collimated beam, which does not allow to directly compare this absorption coefficient with the geometrical light-trapping limit of $4n^2$.

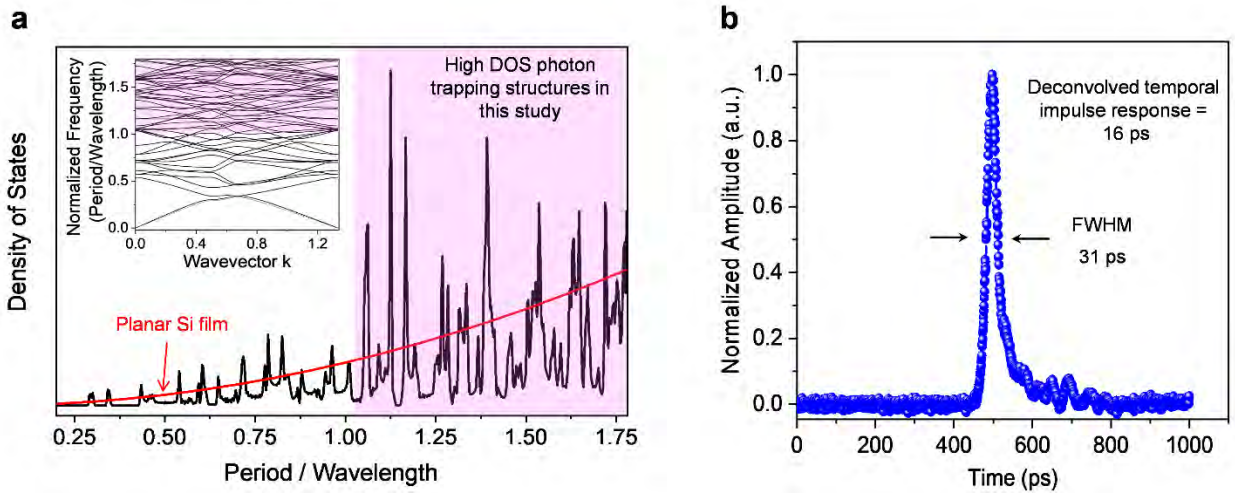

Figure S13: **High density of states and ultrafast time response of photon-trapping photodetectors.** (**a**) Normalized energy band structure of photon-trapping photodetectors with a hole diameter and period ratio (*d/p*) of 0.7 (inset) and the corresponding density of states (DOS), where high peaks in the DOS are observed for frequency (period/wavelength) points higher than 1.0 (shaded region). The red line shows the DOS for the planar devices. (**b**) The 1000 nm thin fabricated MSM photodetector exhibits an ultra-fast time response of 31 ps in full width at half maximum (FWHM). The actual time response of the device is approximated to be ~16 ps by considering 22 ps and 15 ps FWHM response for the 20 GHz sampling oscilloscope and optical laser pulse width, respectively.

3. Ultrafast response measurement:

The high-speed characterizations of the fabricated metal-semiconductor-metal photodetectors were performed by an approx. 15 ps pulse width pulsed laser with a repetition rate and incident wavelength of 70 MHz and 850 nm, respectively, on a microwave probe station. The photocurrent

of the tested photodetectors with a 50 μm diameter was maximized by aligning the center of the optical light beam with a translational stage, while the active region was mainly targeted to be hit by the pulse of the single-mode fiber tip on the probe stage. The input and output power were set at around 1 mW and 100 μW, respectively. In this case, a 20 GHz sampling oscilloscope was utilized to observe the resulting photoresponse of the photodetectors as the electrical pulses, while a 25 GHz bias-T was used for the DC biasing of the photodetectors.

The high-speed pulse response of a photon-trapping photodetector is depicted in Fig. S9 (b) for the incident wavelength of 850 nm. The full width at half maximum (FWHM) for the photon-trapping Si photodetectors is measured to be ~31 ps. However, the actual time response of the device is approximated to be ~16 ps by considering 22 ps and 15 ps FWHM response for the 20 GHz sampling oscilloscope and optical laser pulse width, respectively, which is a valid approximation for our actual measurement with Gaussian pulses.

4. A physics-based explanation for the performance enhancement

We investigated the energy band structure and the corresponding density of states of the photon-trapping photodetector as shown in Fig. S9 (a). The optical density of states (DOS) influences photon absorption in optoelectronic devices. Herein, the ratio of hole diameter and period of the photon-trapping photodetectors is assumed to be $d/p \approx 0.7$, which is consistent with the fabricated devices. The frequency of the energy band diagram was normalized by $2\pi c/p$ so that the values represent period/wavelength, where c and p are the light velocity and the lattice period, respectively. Furthermore, the wavevector is also normalized by $2\pi/p$. The density of states is calculated as an integral over the wavevector for a given frequency. DOS for photodetectors with planar surfaces (without nanoholes) is also added to Fig. S9 (a) as a reference (red curve). First,

the DOS of the photon-trapping photodetectors is found to be higher than that of the photodetectors with planar (flat) surfaces. Then the photodetectors with nanohole periods shorter than the incident wavelengths exhibit distinctly low DOS as compared to the periods which are comparable and/or slightly longer than the wavelengths. For instance, the photonic DOS for a nanohole period of 450 nm and an incident wavelength of 850 nm ($p/\lambda \sim 0.53$) is determined to be distinctly poor. However, our designed and fabricated devices match more with the shaded area on the right part, exhibiting high DOS for the frequency points higher than 1.0 (periods are comparable to and/or slightly longer than the incident wavelengths). Nevertheless, the region with high values of p/λ needs more Fourier components, and the maximum peaks of the DOS are not as pronounced as expected, while there is a constant increase of the optical mode density with p/λ.

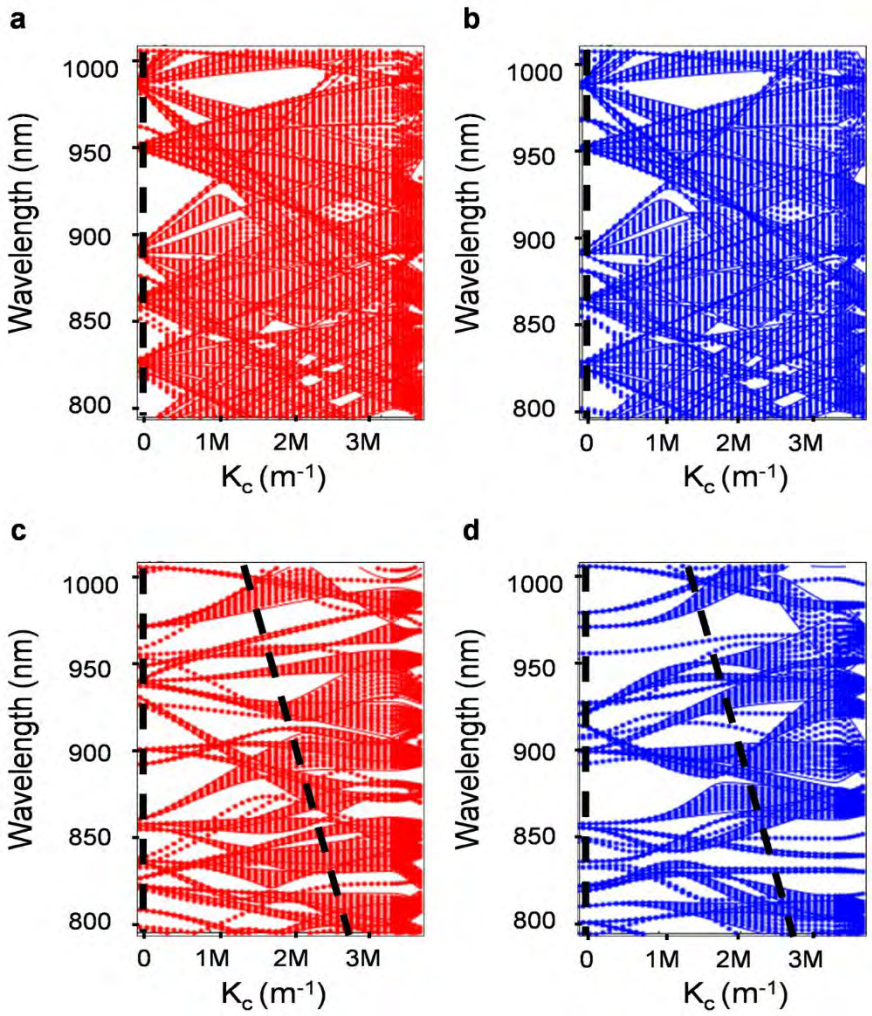

Figure S14: **Simulated band structure of photon-trapping silicon structures.** (**a**) Band structure for photon-trapping structure with a diameter (d) = 100 nm, periodicity (p) = 1000 nm, Si thickness (t_{Si}) = 1000 nm, TE polarization, (**b**) Band structure for photon-trapping structure with diameter = 100 nm, periodicity = 1000 nm, thickness = 1000 nm, TM polarization, (**c**) Band structure for photon-trapping structure with diameter = 700 nm, periodicity = 1000 nm, thickness = 1000 nm, TE polarization, (**d**) Band structure for photon-trapping structure with diameter = 700 nm, periodicity = 1000 nm, thickness = 1000 nm, TM polarization. Slanted dash lines are solutions for k_c that couple into the lateral propagation for a vertically illuminating light source. Small holey structures exhibit solutions only for the finite number of the eigenmodes with $k=0$ (vertical dashed

line), while large holey structures essentially have both solutions $k=k_c$ and $k=0$ (vertical and slanted dash lines) with the eigenmodes, pronouncing enhanced coupling phenomena and laterally propagated optical modes.

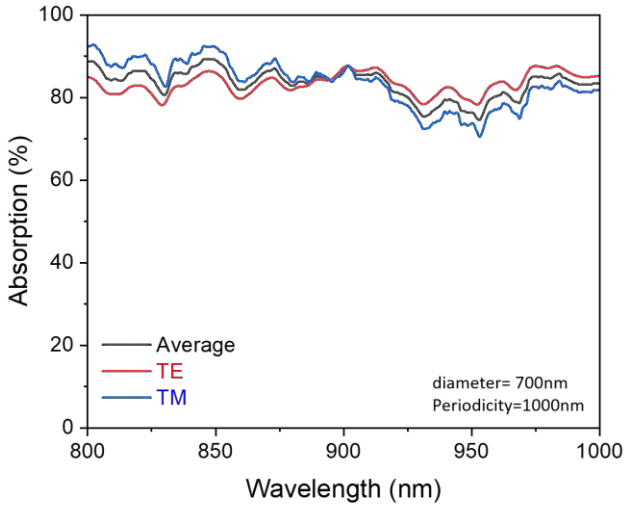

Figure S15: Simulated absorption plots of one-micrometer-thick photon-trapping silicon under TM and TE polarizations. The diameter and periodicity of the microholes were chosen as 700 nm and 1000 nm, respectively.

While the band diagram provides the eigenmodes in the lateral propagation, the coupling from the vertical incidence into the lateral could be described in the model of coupling the light into one hole. The holes have a size comparable with the incident wavelengths and the light forms the modes inside each hole. The FDTD simulations show that the light couples into the hole and leaks into Si, as shown in Fig. S11 (b). The field in each hole could be described as a propagation along the hole with complex wave vector β and lateral wave vector $q_1^2 = (n_1 k_0)^2 - \beta^2$ inside the hole with

$n_1 = 1$ for air and $k_0 = 2p/l$ and $q_2^2 = (n_2 k_0)^2 - \beta^2$ outside the hole where n_2 is the complex refractive index of Si.

The condition for the optical coupling into the eigenmodes of the array can be derived from the conditions when the eigenmode of the hole array $k = q_2$. When the diameter of the holes is small, we will have one possibility of light coupling for the vertical incidence where k is very small or $k = 0$; this happens when the incidence light is nearly vertical. As we can see in Figs. S10 (a-b), there are not many eigenmodes for the coupling. However, if the hole size is comparable to the incident wavelength, the light can couple into the holes and leak out through the sidewalls of the holes, as we can see in Figs. S10 (c-d). In the case of the hole diameter being considerably smaller than the incident wavelength, there is no light coupling into the holes.

The large diameter holes (hole diameter is comparable to the incident wavelength) result in the light leaking laterally into the Si between the holes. From the boundary conditions, it will be possible only if β inside the hole and outside the hole are equal. The conditions when the significant lateral field component will be produced can be found in the cylindrical coordinates for a hole with radius a, and k_0 is the wave vector for a given frequency in a vacuum, n, and e are the refractive index, and dielectric constant of the Si, respectively.

To find the solution for the single hole, we solve Maxwell's equations for the field in the cylindrical coordinates r, θ, and z along the hole axis in the form:

$$E = R(r)\Theta(\theta)e^{-i\beta z} \tag{S1}$$

In this case, the wave equation is:

$$\frac{\partial^2 E_z}{\partial r^2} + \frac{1}{r}\frac{\partial E_z}{\partial r} + \frac{1}{r^2}\frac{\partial^2 E_z}{\partial \theta^2} + (k^2 n(r,\theta)^2 - \beta^2)E_z = 0 \tag{S2}$$

The intensity along the hole decays and it is described by the imaginary part of β. The solution inside and outside the hole is the Bessel function. The solution outside the hole is also described by the Bessel functions of the first kind with complex q_2 that takes into account the absorption in Si. In the case when the absorption of the Si is small, only the real part of q_2 can be considered. As one can see from the FDTD simulations Fig. S11 it is not evanescent as it is for the field approximation in an optical fiber. Matching the boundary conditions at the boundary of the hole, we have the following dispersion equation:

$$\left(\frac{J_n'(q_1a)}{q_1J_n(q_1a)}+\frac{J_n'(q_2a)}{q_1J_n(q_2a)}\right)\left(\frac{k_0^2J_n'(q_1a)}{q_1J_n(q_1a)}+\frac{\varepsilon k_0^2J_n'(q_2a)}{q_1J_n(q_2a)}\right)=\left(\frac{\beta n}{a}\right)^2\left(\frac{1}{q_1^2}+\frac{1}{q_2^2}\right)^2 \quad \text{(S3)}$$

$$k_0=\frac{2\pi}{\lambda},\ q_1^2=k_0^2-\beta^2, q_2^2=\varepsilon k_0^2-\beta^2 \quad \text{(S4)}$$

Where J is the first kind of Bessel function. The solution $q_2 = k_c$ of the equation provides us with the lateral wave vectors in Si that are coupled with eigenmodes. The crossing points of the solution $k = k_c$ or $k = 0$ with the eigenmodes give us the modes that propagate laterally and have been absorbed in the Si. For the small diameter holes, we have the solutions only for the finite number of the eigenmodes with $k = 0$, which corresponds to the guided modes in photonic crystals. They produce sharp spikes in absorption, as shown in Fig. (4d). In the case of the large-diameter holes, there is a continuous solution for any wavelength in the range of interest between 0.8 and 1 μm. In addition to that, they have small group velocity u_g that also increases the absorption with more extended light-matter interaction.

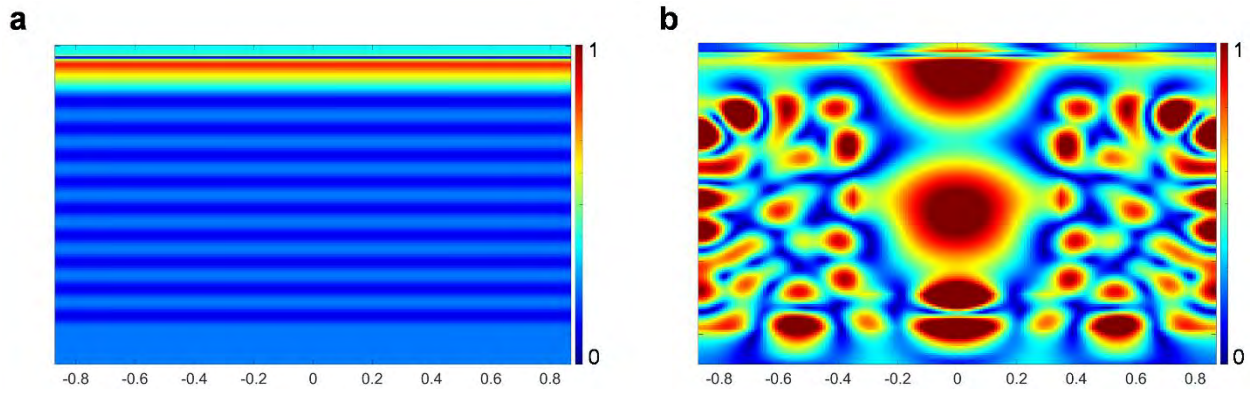

Figure S16: **Electromagnetic field distribution mapping in planar and holey photon-trapping structure**. FDTD optical simulation for light coupling in (**a**) Planar and (**b**) Photon-trapping Si photodetector on SOI.

Table. S1: **Performance comparison of high-speed silicon photodiodes for optical communications.** Photo sensitivities or quantum efficiencies and approximated bandwidth of the fabricated photodetectors for a broadband spectrum in the near-infrared are also included as a comparison.

Ref.	Device type	Responsivity (A/W) or EQE	Wavelength (nm)	Bandwidth (GHz) or data rate (Gb/s)	CMOS compatibility and other challenges
Si[44]	p^+-p-n avalanche	0.74 A/W (at 823 nm)	850	1.6 GHz, 3.5 Gb/s	0.18 µm CMOS technology
Si [60]	p^+-n-p	N.A.	850	3 Gb/s with an analog equalizer	0.18 µm CMOS technology
Si [61]	Resonant cavity *pin*	40 % EQE	860	10 Gb/s	Complex cavity mirror fabrication
Si [62]	Resonant cavity *pin*	40 % EQE	822	10 GHz, >10 Gb/s	Complex cavity mirror fabrication
Si [63]	MSM	N.A.	850	2.5 GHz	CMOS compatible

Si [64]	lateral *pin*	47% internal QE	840	NA.	CMOS compatible
Si[65]	lateral *pin*	0.32 A/W (from 4 PDs)	850	10 Gb/s with TIA	0.13 µm CMOS technology
Si [66]	vertical *pin*	0.26 A/W	850	Could be 11 Gb/s with equalizer	Modified 0.5 µm BiCMOS technology
Si [67]	vertical *pin*	52% EQE at 850 nm	broadband absorption between 800-900 nm	>10 GHz	CMOS compatible
Si [68]	APD	0.07 A/W	850	5 GHz, 12.5 Gb/s with equalizer circuit	0.25 µm Si/Ge BiCMOS technology
Si [68]	APD	10% EQE	850	8 Gb/s	0.13 µm CMOS technology
Si[69]	APD (double PD)	0.84 A/W	850	0.7 GHz	40 nm CMOS technology
Si[70]	Spatially-modulated APD	0.18 A/W	850	8 GHz, 12.5 Gb/s with TIA, equalizer and limiting amplifier	0.13 µm CMOS technology
Si[71]	APD	4.67 A/W	850	10 Gb/s	0.13 µm CMOS technology
Si[72]	APD	2.94 A/W	850	3.2 GHz	65 nm CMOS technology
Si[73]	SPAD	PDP <10% at 850 nm	850	Sub-40ps gate shifts	Standard CMOS technology
Si[74]	SPAD	PDP <5% at 850 nm	850	160 ps FWHM	0.35 µm CMOS technology
Si[75]	Lateral PIN	36.8% (theoretical 77%)	850	11.3 GHz	
Si-Ge[76]	PIN	-	1550	60 GHz	16 nm CMOS technology
Graphene-Si [77]	Graphene PIN	35 mA/W (~70% visible)		65 GHz (3-dB cutoff)	CMOS compatible

Nano-structured Si [48]	SPAD	32% PDE*	850	25 ps (FWHM)	CMOS compatible
Si **[This work]**	MSM	86% EQE at 850 nm (1 μm thin Si)	broadband absorption between 800-940 nm	>16 GHz Ultimate BW (50μm device)	CMOS compatible (Monolithic Integration)
Si **[This work]**	MSM	72% EQE at 905 nm (1 μm thin Si)	broadband absorption between 800-940 nm	>16 GHz Ultimate BW (50μm device)	CMOS compatible (Monolithic Integration)
Si **[This work]**	MSM	32% EQE at 940 nm (1 μm thin Si)	broadband absorption between 800-940 nm	>16 GHz Ultimate BW (50μm device)	CMOS compatible (Monolithic Integration)

Movie S1: Demonstration of bending normally incident beams of light by almost ninety degrees and transformed into laterally propagating modes of light along the plane of the silicon film integrated with engineered an array of periodic photon-trapping structures. Such surface structures effectively increase the propagation length of light, contributing to more than an order of magnitude improvement in light absorption efficiency in photodetectors.

Movie S2: Propagation of light in both silicon planar (left) and photon-trapping (right) photodetectors for the incident wavelength of 850 nm. Most of the light incident on the planar device either reflects from the surface or passes through it and cannot efficiently absorb in the silicon, whereas light incident on the photon-trapping structures bends almost at a right angle into laterally propagating modes of light along the plane of the Si absorber layer. The photon-trapping surface structure reduces the surface reflection, enhances the confinement of light within the silicon absorber layer, and increases the light-matter interaction. Such photon-trapping structure in one-micron silicon facilitates very high photoabsorption as well as ultrafast time response.

Movie S3: Optical propagation of light in 30 nm ultra-thin silicon with integrated photon-trapping structure. Similar to the Si film with 1000 nm thickness, photon-trapping ultra-thin Si film exhibits dramatically higher absorption efficiency than the planar Si film. More than 8% absorption efficiency can be obtained, while it is less than 1% in such planar silicon. Such ultrathin Si-based photo-trapping-equipped photodetectors are intriguingly encouraging for the fabrication of ultrafast photodetectors in the existing CMOS foundry framework.